https://doi.org/10.1016/j.istruc.2024.106389

Numerical investigation and design of a demountable steel connection system for precast concrete pavements

Jiachen GUO[1], Tak-Ming CHAN[1,*]

[1] Department of Civil and Environmental Engineering, The Hong Kong Polytechnic University, Hong Kong, China

* Corresponding author: tak-ming.chan@polyu.edu.hk

Abstract:

Jointed precast concrete pavement systems (JPrCP) are hard to be reused after installing steel dowel bars. To improve the reusability of precast pavement units, a demountable steel connection system is proposed. This paper presents a comprehensive finite element analysis (FEA) on models equipped with this connection system under vertical load. Parameters including the thickness, width, end distance and length of the steel plate, the height of the steel bar connection and the grade of high-strength bolts were studied. The FEA results indicated that the steel plate end distance, the height of the steel bar connection and the grade of high-strength bolts affected the ultimate load of the connection system. The prying force between the steel bar connection and plate was lowered by increasing the steel plate length, the steel bar connection height and reducing the steel plate end distance. For preventing the necking of high-strength bolts which impaired the reusability of precast units, analytical solutions were derived to predict the design load of the steel connection system. Finally, according to the obtained data, design recommendations were proposed to improve the demountable connection design.

Keywords: demountable steel connection system, parametric analysis, failure mode, ultimate load, analytical solutions, design recommendations.

1. Introduction

With the rapid growth of national economy, the acceleration of urbanisation gained a widespread concern around the world [1]. As one of the primary branches of urban infrastructure, current municipal road systems always suffer unavoidable damages due to the dramatic increase in traffic volume [1-5]. However, because of long-time traffic closure, existing pavement maintenance and rehabilitation have brought huge challenges for traffic agencies [1, 2, 6, 7]. Cookson [8] carried out a statistical analysis among European countries and stated that the overall expense caused by traffic congestion was expected to exceed 160 billion Euros by 2025. Although the application of fast-maintenance materials like asphalt and early-strength concrete can reduce the period of traffic closure, repaired pavements are often subjected to premature damages [9]. Therefore, to balance the contradiction between high durability and fast construction, precast concrete pavement (PCP) technology is recommended and has been widely applied in pavement rehabilitation and new pavement construction [9-11]. According to the traffic data collected by the Missouri Department of Transport, the application of precast concrete pavement (PCP) technology could reduce the traffic closure-related cost by 25 percent [12, 13]. Compared with cast-in-situ concrete, the advantages of PCP technology are introduced as follows:

- High quality of PCP panel: well-graded aggregates and the controlled water-to-cement ratio ensure sound workability and homogeneity of concrete [1, 7, 9];
- Better curing condition: after concrete casting, PCP units are cured under controlled temperature and moisture [2, 14, 15];
- Less weather and climate restrictions: onsite concrete casting is hard to be carried out in cold and rainy environments. While PCP units are cast in fabrication plants which are not affected by temperature and climate changes [1, 6, 7, 11];

- Short traffic closure: onsite concrete curing is not required after applying PCP technology. The fast installation of PCP units minimises the duration of traffic closure [11, 16, 17];
- Low maintenance cost and high durability: due to great wear resistance and excellent quality, the service life of PCP systems is extended, thereby reducing the maintenance cost [1, 7, 16, 18].
- Low safety risks: road users and construction workers are less exposed to construction sites. Therefore, construction related safety risks are reduced [19-21].

In addition, the design of pavement joints also requires a significant consideration because of the discontinuity at joint locations. Epoxy-coated steel dowel bars are installed along transverse joints of jointed precast concrete pavement (JPrCP) systems to connect pavement slabs and achieve an effective load transfer. However, after millions of load repetitions, epoxy coating on dowel bars can easily deteriorate, thereby leading to corrosion-related issues. Fig. 1 shows corroded dowel bars observed from field applications [1, 22]. To protect dowel bars from corrosion, corrosion-free materials such as stainless steel and fibre reinforced polymer (FRP) were adopted to fabricate dowel bars [23-27].

(a) (b)

Fig. 1. Dowel bar corrosion (a) corroded dowel bars embedded in concrete [22], (b) corroded dowel bars [1].

To investigate the complex behaviour of dowel bars embedded into concrete under vertical load, finite element analysis (FEA) is always adopted. The load transferred characteristic between pavement slabs can be simulated by two-dimensional and three-dimensional modelling techniques as introduced below:

Two-dimensional finite element analysis

- Discrete dowel bars and concrete pavement slabs are modelled by beam elements and two-dimensional plate elements, respectively. The interaction between dowel bars and concrete is simulated via contact elements [28].
- Concrete pavements are modelled by two-dimensional plate elements. Spring elements are placed between pavement slabs to simulate the pavement load transfer [29-31].
- Two-dimensional plate elements and beam elements are used to model concrete pavements and dowel bars, respectively. Vertical spring elements with a stiffness equal to the modulus of dowel support are adopted to model the dowel-concrete contact behaviour [32-35].

Three-dimensional finite element analysis

- Three-dimensional solid elements are used to model concrete pavements and beam elements are optioned to model dowel bars. Separated spring elements are set between dowel bars and concrete pavement to simulate the dowel-concrete interaction [36-39].
- Both concrete pavements and dowel bars are modelled by three-dimensional solid elements. The surface-to-surface contact modelling technique is applied to model the interaction between dowel bars and surrounding concrete [27, 40-45].

Although two-dimensional FEA requires less computational efforts, the accuracy of this approach cannot match that of three-dimensional FEA. Components modelled by three-dimensional solid elements together with the surface-to-surface contact modelling are the most accurate way to reproduce the load transfer between pavement slabs [40, 44, 45].

Although steel dowel bars are widely used in practice, they are difficult to be dismantled after

installation. To address this issue, a demountable steel connection system which consists of a steel bar connection and embedded steel plates connected by high-strength bolts was developed. In comparison with traditional pavement connections, this steel bar connection can be flexibly installed and dismantled, thereby allowing it to be applied in different scenarios and further improving the reusability of PCP slabs. As a result, the excellent durability of precast concrete components can be maximised, and the production of construction waste can be minimised [46]. However, because only a limited number of specimens were tested, it was impossible to comprehensively evaluate parameters that influenced the structural performance of this demountable steel connection system. The main objective of this research is to implement a comprehensive parametric analysis on this novel connection system through FEA. Based on the deformation of each steel component, the analytical models to predict the design load of the connection system are derived and verified. By using the obtained FEA data, design recommendations are finally proposed to instruct the design of this demountable steel connection system.

2. Finite element analysis

2.1. Test specimens

The configuration of the demountable steel connection system is shown Fig. 2(a), including the steel bar connection and the steel plates connected by high-strength bolts. Both the steel bar connection and plates were made of austenitic stainless steel to improve their corrosion resistance. Once high-strength bolts are removed, individual pavement units and the steel bar connection can be directly reused for different applications. To evaluate the structural behaviour of the proposed demountable steel connection system, monotonic loading tests were conducted [46]. Fig. 2(b) introduces the test specimen

that consists of the loaded block and the reaction block with a embeded steel plate. The steel bar connection is connected to the embedded steel plates via slots on the top surface of concrete blocks. These slots are then filled with asphalt material to prevent water from penetrating into the embedded steel plates and the corrosion of high-strength bolts. When precast cocnrete units need to be reused, asphalt material is firstly melted by heat and then the steel bar connection can be disassmebled.

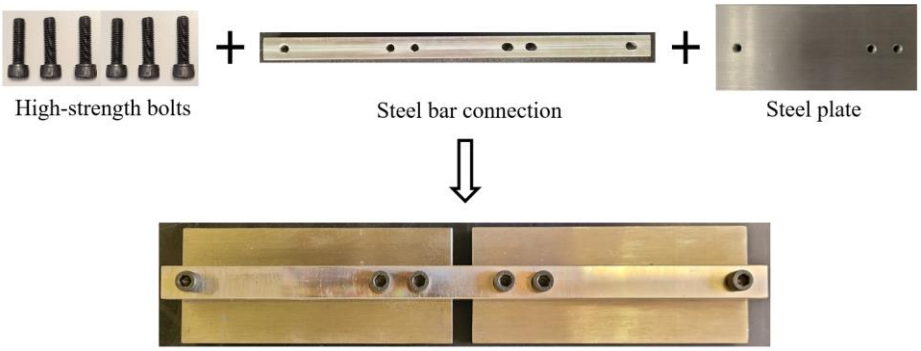

Demountable steel connection system

(a)

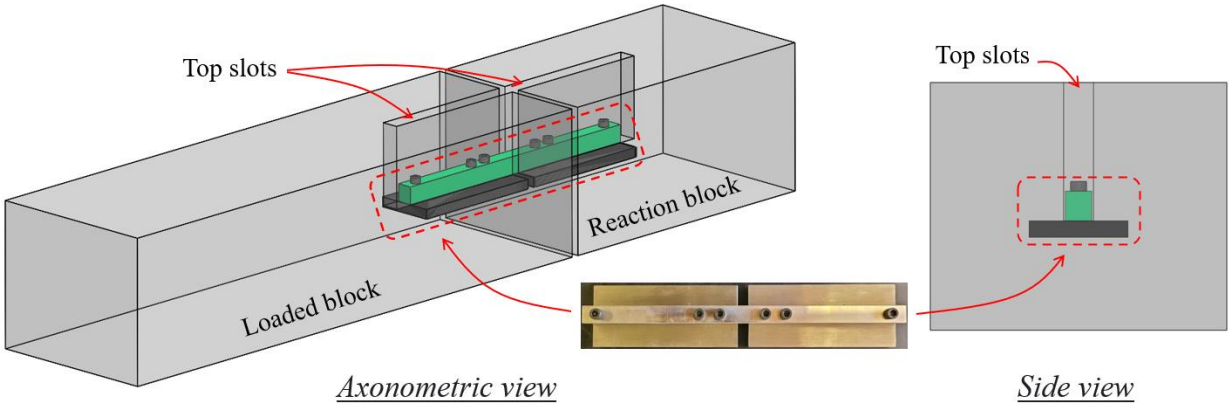

Precast concrete blocks with demountable steel connection system

(b)

Fig. 2. Demountable steel connection system (a) components, (b) test specimen.

Among discrete pavement connections installed along the transverse joint, the critical connections under wheels transfer the largest vertical load and always suffer premature damages within pavement service life. As a result, to investigate the structural performance of the proposed steel connection system, it is reasonable to focus on the behaviour of an individual connection and identify its load transfer characteristic. Furthermore, the presence of pavement subbase only influences the magnitude

of the transferred load rather than affects the load transfer capacity of the connection. Therefore, in the test method recommended in AASHTO T253 [47], pavement subbase is not included, and the vertical load transferred by the connection can be directly obtained. Fig. 3(a) introduces the width and thickness of the concrete blocks, which is determined according to the common concrete pavement thickness and dowel bar spacing after considering the scale factor of 0.6 [48]. As displayed in Fig. 3(b), the length of the 10 mm thick steel plate was the same as the embedded depth of scaled dowel bars and equal to 140 mm. Locations of high-strength bolts could also be identified, in which the first two bolts B1 and B2 were designed to transfer the vertical load, while the third bolt B3 was installed to fix the steel bar connection. The end distance e_1 of the steel plate, namely the distance between the position of the first bolt and the joint surface, was designed to be 15 mm or 30 mm in experiments. Two different types of steel bar connections with a "narrow" section (16 mm × 18 mm) or "wide" section (22 mm × 13 mm) were adopted. Fig. 3(c) shows the setup for testing this demountable connection system. To prevent unexpected upward deformations, the reaction block was clamped to the rigid block via a fixing device. The loaded block was supported by a roller located 500 mm from the joint surface. A displacement-controlled vertical load was applied to a steel block placed next to the joint surface to minimise the induced flexural deformation of the loaded block.

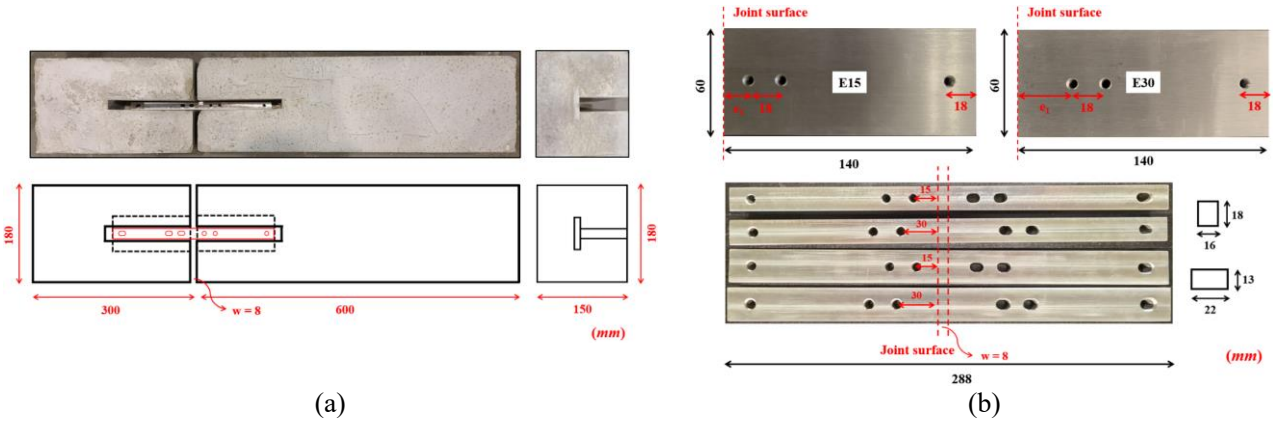

(a) (b)

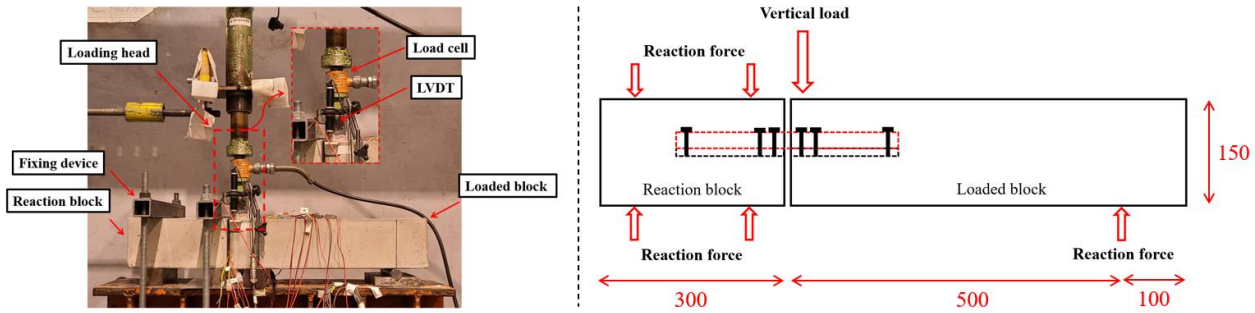

(c)

Fig. 3. Specimen configuration and test setup (a) concrete block, (b) steel bar connection and plate, (c) test setup.

2.2. Finite element model

The finite element modelling of concrete pavement blocks with the demountable steel connection system was carried out by ABAQUS [49]. Fig. 4(a) to (d) introduces the components of the developed model which were modelled by three-dimensional solid elements with reduced integration (C3D8R). After carrying out the mesh sensitivity analysis, 4 mm sized elements were adopted to model the steel plate and steel bar connection. Because localised concrete failure primarily happened at the joint surface of concrete blocks, the refined mesh with a size of 4 mm was also assigned in the part concrete blocks near the joint surface. While in the region away from the joint, 15 mm sized elements were used to reduce the total number of elements and minimise the computational time. Because high-strength bolts are critical components that governed the ultimate load of the steel connection system, the mesh size along the bolt shank was set to 1 mm to reproduce the typical failure. To simplify the developed finite element model, the role of the fixing device was achieved by restraining the bottom surface of the reaction block as described in Fig. 5(a). In terms of the roller support modelling, as shown in Fig. 5(b), a coupling constraint was assigned to the reference point RP-1 in an elastic plate which was attached to the bottom surface of the loaded block. Fig. 5(c) displays the vertical load arrangement applied via a coupling constraint to the reference point RP-2 in the steel block near the joint surface.

Since thread stripping failure was not observed in experimental tests and could be prevented when the thickness of the stainless steel plate was greater than the bolt diameter [50], the grip effect between the high-strength bolts and the steel plate was simulated by a tie constraint as shown in Fig. 6 [51]. The threaded bolt shank was simplified with a reduced section area determined according to EN ISO 898-1 [52].

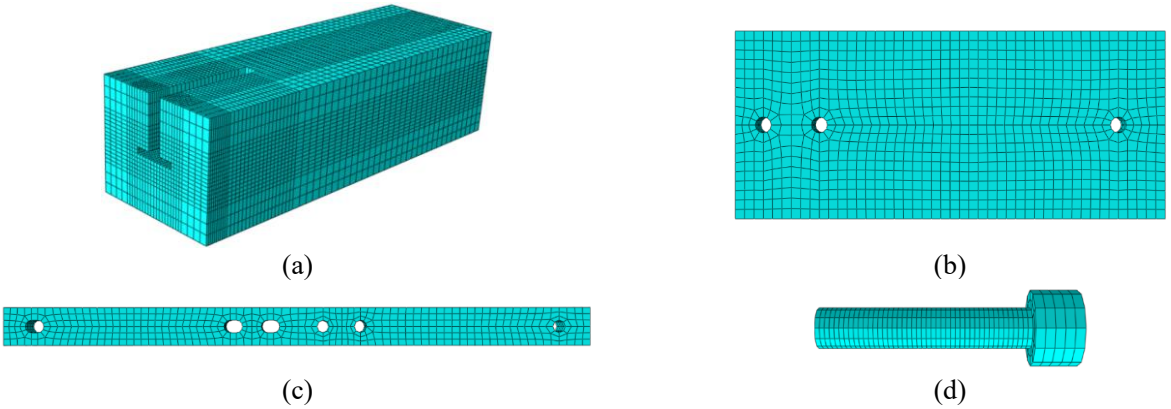

Fig. 4. Finite element model (a) concrete block, (b) steel plate, (c) steel bar connection, (d) high-strength bolt.

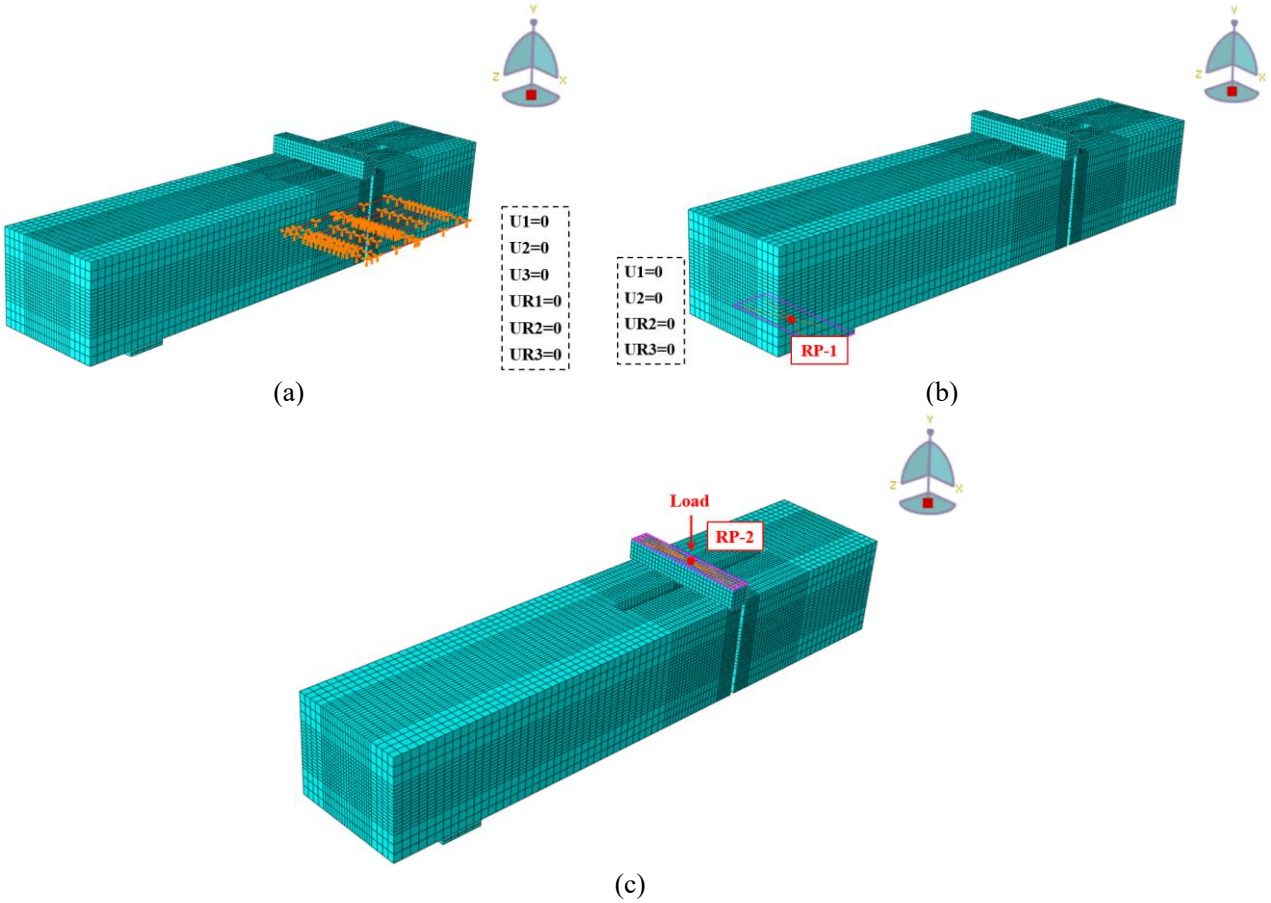

Fig. 5. Boundary conditions and load arrangement (a) fixing device simulation, (b) roller support simulation, (c) vertical load arrangement.

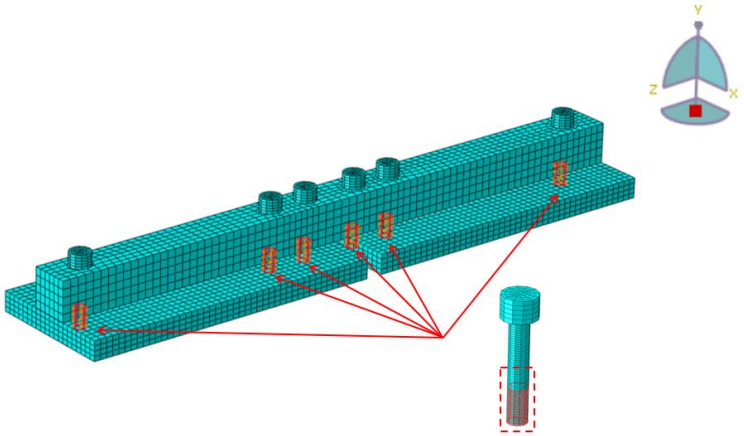

Fig. 6. Thread grip effect simulation.

Regarding the contact simulation, the interaction between different components was defined by establishing contact pairs. With the application of the surface-to-surface contact modelling technique, the normal contact behaviour was defined by the 'hard' contact and the tangential behaviour was modelled by the 'penalty' friction formulation. The frictional coefficient between steel and concrete was set to 0.35 as recommended by Al-Humeidawi et al. [44]. Because the steel components were lubricated by oil before installation, the frictional coefficient between these components was calibrated to 0.2 after fitting to test results.

2.3. Materials

2.3.1. Concrete

The concrete damaged plasticity (CDP) model available in ABAQUS was used to capture the compressive and tensile behaviour of concrete [53, 54]. For the uniaxial compressive behaviour, a linear stress-strain relationship was defined before $0.4f_c$ and followed by a nonlinear stage as expressed by Eqs. (1) to (3) recommended in CEB-FIP Model Code 2010 [55], where, σ_c is the compressive stress; f_c refers to the cylinder compressive strength; ε_c is the compressive strain; ε_{c1} denotes the

compressive strain at the cylinder compressive strength; $\varepsilon_{c,lim}$ is the limited compressive strain at $0.5f_c$ within the post-peak stage; E_{ci} represents the tangential modulus of elasticity at the origin; E_{cl} indicates the secant modulus of elasticity at f_c; k is the plasticity number. For the descending stage beyond $\varepsilon_{c,lim}$, the stress-strain relationship proposed in CEB-FIP Model Code 1990 [56] was considered as indicated in Eqs. (4) and (5). Material properties collected from uniaxial compression tests are summarised in Table 1, in which E_c is the secant modulus of elasticity at $0.4f_c$.

$$\frac{\sigma_c}{f_c} = \left[\frac{k\eta - \eta^2}{1+(k-2)\eta}\right] \quad (\varepsilon_c \le \varepsilon_{c,lim}) \tag{1}$$

$$\eta = \left(\frac{\varepsilon_c}{\varepsilon_{cl}}\right) \tag{2}$$

$$k = \left(\frac{E_{ci}}{E_{cl}}\right) \tag{3}$$

$$\sigma_c = \left[\left(\frac{1}{\frac{\varepsilon_{c,lim}}{\varepsilon_{cl}}}\xi - \frac{2}{(\frac{\varepsilon_{c,lim}}{\varepsilon_{cl}})^2}\right)\left(\frac{\varepsilon_c}{\varepsilon_{cl}}\right)^2 + \left(\frac{4}{\frac{\varepsilon_{c,lim}}{\varepsilon_{cl}}} - \xi\right)\left(\frac{\varepsilon_c}{\varepsilon_{cl}}\right)\right]^{-1} f_c \quad (\varepsilon_c > \varepsilon_{c,lim}) \tag{4}$$

$$\xi = \frac{4\left[(\frac{\varepsilon_{c,lim}}{\varepsilon_{cl}})^2\left(\frac{E_{ci}}{E_{cl}} - 2\right) + 2\frac{\varepsilon_{c,lim}}{\varepsilon_{cl}} - \frac{E_{ci}}{E_{cl}}\right]}{\left[\frac{\varepsilon_{c,lim}}{\varepsilon_{cl}}\left(\frac{E_{ci}}{E_{cl}} - 2\right) + 1\right]^2} \tag{5}$$

Table 1 Material properties of concrete (uniaxial compression).

f_c (MPa)	ε_{cl}	E_{ci} (GPa)	E_{cl} (GPa)	E_c (GPa)	k
34.45	0.0024	29.6	14.4	26.2	2.06

In terms of the uniaxial tensile behaviour of concrete, CEB-FIP Model Code 2010 [55] recommended a tensile stress-crack width relationship as expressed by Eqs. (6) to (10), where, σ_{ct} and f_t refer to tensile stress and uniaxial tensile strength of concrete; w, w_t and w_c represent the crack width, the transition crack width and the crack opening width, respectively; G_F is the fracture energy of concrete. After

obtaining the splitting tensile strength f_t, other parameters were computed as listed in Table 2.

$$\sigma_{ct} = f_t\left(1.0-0.8\frac{w}{w_1}\right)\ (w \le w_t) \tag{6}$$

$$\sigma_{ct} = f_t\left(0.25-0.05\frac{w}{w_1}\right)\ (w_t < w \le w_c) \tag{7}$$

$$G_F = 0.73(f_c)^{0.18} \tag{8}$$

$$w_t = \frac{G_F}{f_t} \tag{9}$$

$$w_c = \frac{5G_F}{f_t} \tag{10}$$

Table 2 Material properties of concrete (uniaxial tension).

f_t (MPa)	G_F (N/mm)	w_t (mm)	w_c (mm)
3.49	0.138	0.0396	0.198

Additionally, to account for the effects of concrete crushing and tensile cracks on stiffness reduction, both the compressive damage and tensile damage variables were incorporated. For the compressive damage variable d_c, it was determined by compressive stress σ_c, plastic strain ε_c^{pl} and inelastic strain ε_c^{in} as expressed by Eqs. (11) and (12) [57]. The tensile damage variable d_t increased as tensile cracks propagated and was determined by Eqs. (13) and (14). Additional parameters of the CDP model including the dilation angle ψ, the equibiaxial compressive stress to uniaxial compressive stress f_{b0}/f_c, the tensile meridian to compressive meridian K, eccentricity and viscosity parameter were obtained from ABAQUS user guide [49], equal to 38°, 1.16, 0.667, 0.1 and zero, respectively.

$$d_c = 1-\frac{\sigma_c E_c^{-1}}{(\varepsilon_c^{in}-\varepsilon_c^{pl})+\sigma_c E_c^{-1}} \tag{11}$$

$$\varepsilon_c^{pl} = 0.7\varepsilon_c^{in} \tag{12}$$

198 $$d_t = \frac{f_t\left(w - 0.4\frac{w^2}{w_t}\right)}{G_F} \quad (w \le w_t) \tag{13}$$

199 $$d_t = 1 - \frac{\left[f_t\left(0.125 - 0.025\frac{w}{w_t}\right)(w_c - w)\right]}{G_F} \quad (w_t < w \le w_c) \tag{14}$$

200 2.3.2. Steel

201 304 austenitic stainless steel was utilised to fabricate the steel plate and the steel bar connection. To
202 acquire the corresponding material properties, tensile coupons extracted from these two components
203 were tested [46]. Fig. 7 plots the stress-strain curves of stainless steel and the obtained material
204 properties are summarised in Table 3. The true stress-strain curve was obtained through the converting
205 equations as indicated in Eqs. (15) and (16), where σ_n and ε_n are nominal stress and nominal strain,
206 respectively; σ_t and ε_t are true stress and true strain, respectively.

207 $$\sigma_t = \sigma_n\left(1 + \varepsilon_n\right) \tag{15}$$

208 $$\varepsilon_t = \ln\left(1 + \varepsilon_n\right) \tag{16}$$

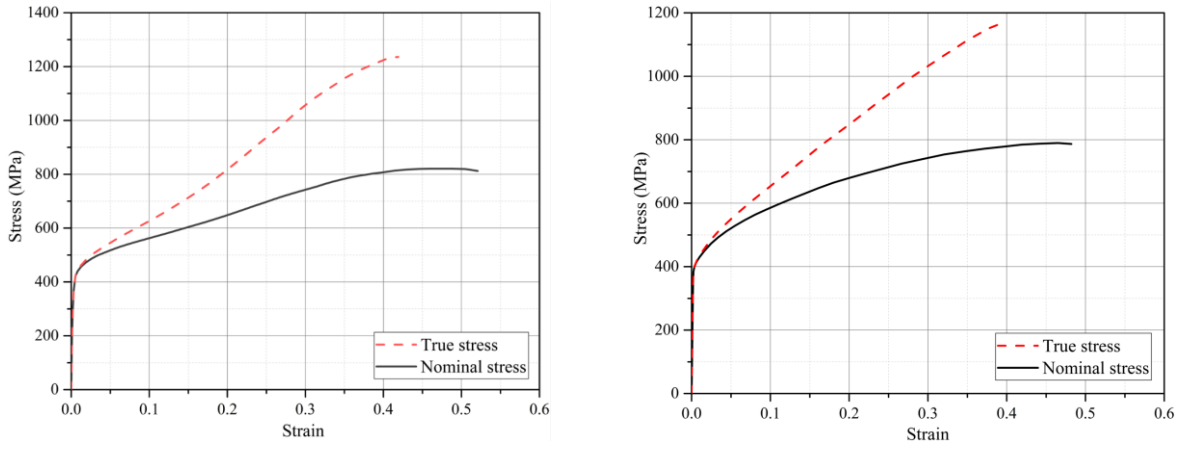

Fig. 7. Stress-strain relationship (a) steel bar connection, (b) steel plate [46].

209 Table 3 Material properties of stainless steel.

Stainless steel	Modulus of elasticity E (GPa)	Yield strength f_y (MPa)	Ultimate tensile strength f_u (MPa)	Fracture strain ε_f
Steel plate	192.5	405	790	0.53
Steel bar connection	190.9	394	821	0.59

2.3.3. High-strength bolt

In experimental tests, 12.9 grade high-strength bolts were used to connect the steel plate and steel bar connection. The stress-strain relationship of the high-strength bolts was obtained through uniaxial tension tests. In the parametric study, 8.8 grade and 10.9 grade high-strength bolts were also involved to further investigate the effect of bolt grades on the structural performance of the proposed connection system. Fig. 8 plots the stress-strain relationships of high-strength bolts and detailed material properies of high-sterngth bolts can be found in Table 4. The stress-strain curves of 8.8 grade and 10.9 grade high-strength bolts were obtained from the research conducted by Song et al. [58] and Li et al. [59], respectively. Because of the non-uniform axial deformation within the necking zone, the post-necking true stress-strain relationship of high-strength bolts were difficult to be plotted. Therefore, on the basis of the FEA conducted by Yang et al. [60], the post-necking true stress-strain curve could be predicted by a power law relationship as expressed by Eq. (17), where, $K=\sigma_{t,u}/n^{n}$; $n=\varepsilon_{t,u}$; $\sigma_{t,u}$ and $\varepsilon_{t,u}$ are the true stress and true strain at the initiation of necking, respectively. Fig. 9 plots the pre-necking and post-necking true stress-strain curves of high-strength bolts.

$$\sigma_t = K\varepsilon_t^n \tag{17}$$

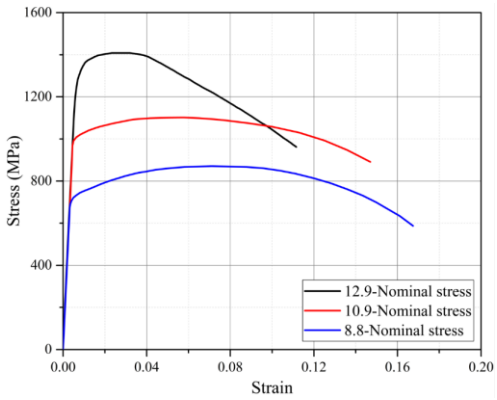

Fig. 8. Stress-strain relationship of high-strength bolts.

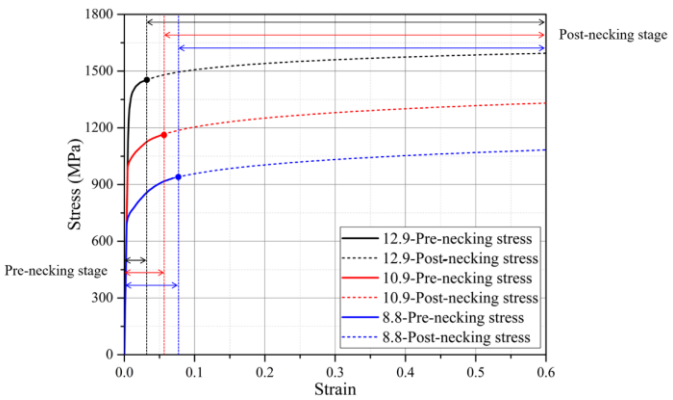

Fig. 9. True stress-strain relationship of high-strength bolts.

Table 4 Material properties of high-strength bolts.

Bolt grade	Modulus of elasticity E (GPa)	Yield strength f_y (MPa)	Ultimate tensile strength f_{ub} (MPa)
8.8	211.1	726	871
10.9	210.0	1013	1102
12.9	211.3	1318	1408

2.4. Model validation

FEA was implemented by the ABAQUS explicit solver that was suggested in the analysis of complex structures to reduce convergent issues. However, owing to the small time increment, FEA with the explicit solver generally required high computational efforts. Therefore, the mass scaling factor (MSF) was incorporated to expand the weight of elements and increase the critical time increment. After comparing the kinetic energy (ALLKE) and internal energy (ALLIE) generated from the ABAQUS history output, the target time increment was adjusted to 1×10^{-5} to minimise the dynamic effect and keep a relatively low computational effort.

Developed finite element models were validated against test results in terms of the failure mode and deflection response. A total of four specimens were tested and each specimen was labelled by the section of the steel bar connection, the width and the end distance of the steel plate [46]. For example, "N60E15" represents the specimen equipped with the "narrow" section connection and the steel plate of 60 mm width and 15 mm end distance. In FEA, as shown in Fig. 10, localised concrete crushing under the steel plate in the reaction block and the bolt necking before fracture in the loaded block were precisely reproduced by the concrete compressive damage variable d_c and the equivalent plastic strain (PEEQ), respectively. In terms of the deflection response, the load-deflection relationships recorded in experimental tests and those generated from FEA are compared in Fig. 11. Because there were small gaps between the steel bar connection and plate during the installation of high-strength bolts, the initial stiffness of test specimens was lower than that of finite element models. However, as summarised in

245 Table 5, the ultimate loads predicted from FEA are in close agreement with those recorded in

246 experimental tests, with a mean value of 1.02 and a coefficient of variation (CoV) of 0.02.

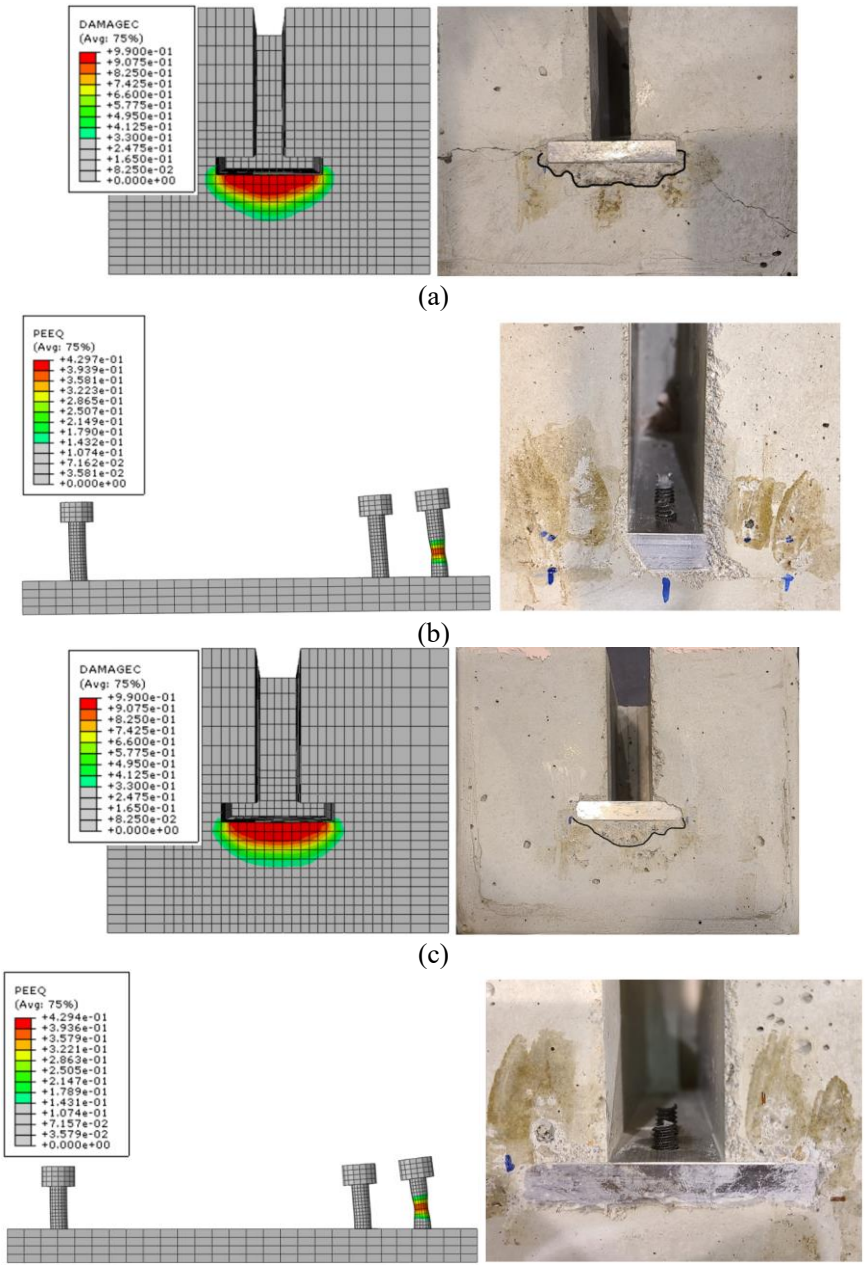

Fig. 10. Localised concrete crushing and bolt necking (fracture) in FEA and tests (a) N60E15-concrete crushing, (b) N60E15-bolt necking and fracture, (c) W60E15-concrete crushing, (d) W60E15 bolt necking and fracture.

247

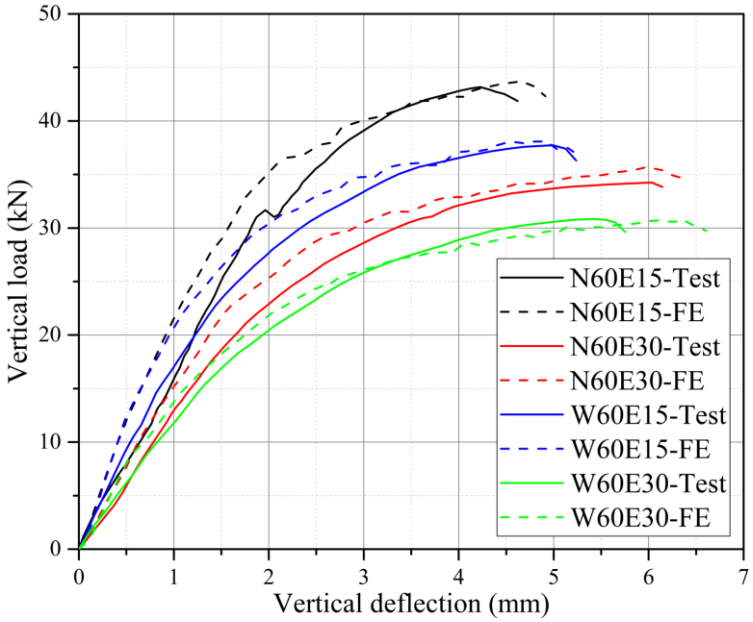

Fig. 11. Load-deflection curves from tests and FEA.

Table 5 Ultimate load comparison between test and FEA.

Specimen ID	$N_{u,Test}$	$N_{u,FE}$	$N_{u,FE}/N_{u,Test}$
N60E15	43.16	43.69	1.01
N60E30	34.25	35.69	1.04
W60E15	37.73	38.09	1.01
W60E30	30.85	30.72	1.00
		Average	1.02
		CoV	0.02

3. Parametric analysis

After conducting the model validation, a comprehensive parametric analysis was conducted with 189 developed models. Parameters including the steel plate thickness (T), width (W), end distance (E), length (L), the height of the steel bar connection (H) and the grade of high-strength bolts were investigated in terms of the failure mode, ultimate load of the demountable connection system and the evolution of the prying force between the steel bar connection and plate. The dimensions of each component and the full-scale model are displayed in Fig. 12, in which the joint width between the loaded and the reaction blocks is 12.5 mm as recommended in design codes [1, 48, 61]. In the parametric analysis, all models were specified by the height of the steel bar connection, the dimension of the steel plate and the grade of high-strength bolts.

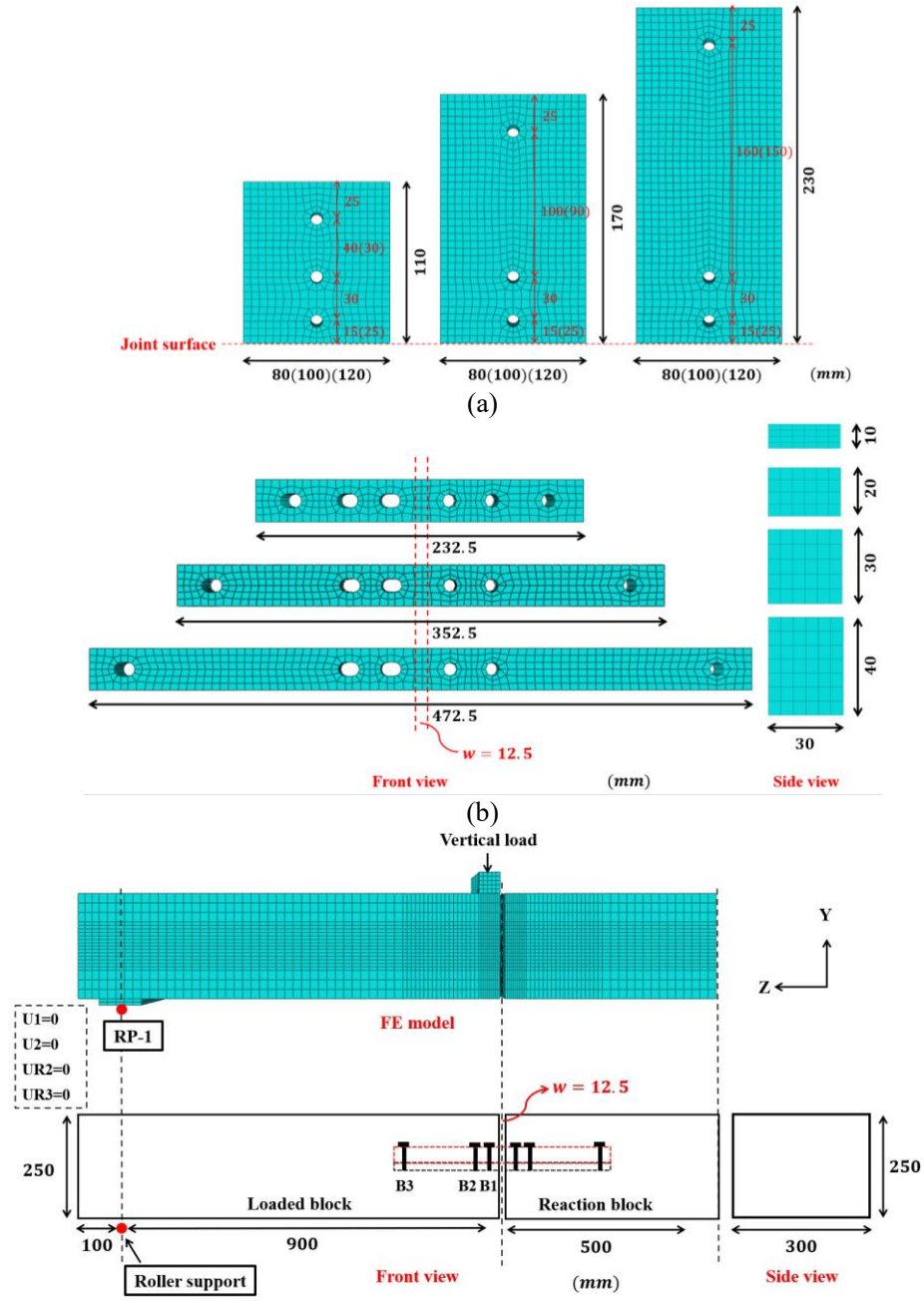

Fig. 12. Dimensions of components and the full-scale model (a) steel plate, (b) steel bar connection, (c) full-scale model.

3.1. Steel plate thickness

In FEA, steel plates with a thickness of 10 mm to 20 mm were involved. Parametric analysis results indicated that the thickness of the steel plate influenced the failure mode of the loaded block. For models equipped with steel plates of a small thickness and flexural stiffness, vertical compressive stress primarily concentrated at the joint surface of the loaded block. This might result in localised concrete

crushing with an increased vertical load as displayed in Fig. 13(a). However, after increasing the plate thickness to 20 mm, the high flexural rigidity of the plate promoted a uniform distribution of contact stress. As a result, the failure of the loaded block was transferred to bolt fracture as shown in Fig. 13(b).

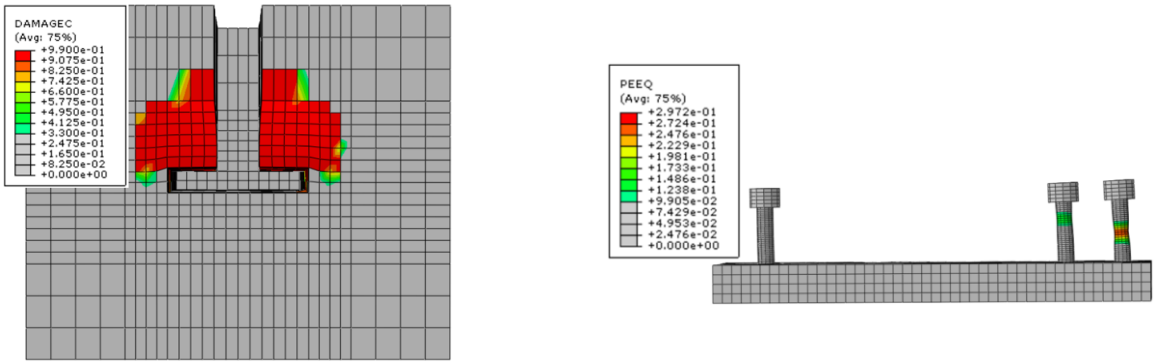

(a) (b)

Fig. 13. Failure modes of models H30-W100T15(20)L230E15-12.9 (a) H30-W100T15L230E15-12.9-concrete crushing, (b) H30-W100T20L230E15-12.9-bolt fracture.

In addition, according to the load-deflection curves plotted in Fig. 14(a), the initial stiffness and ultimate load of the demountable connection system enhanced with an increased steel plate thickness. This might be due to the reduced flexural deformation of the steel plate and the increased axial force generated in high-strength bolts. For the prying force created between the steel plate and connection, it caused the total bolt load to exceed the applied vertical load and could be determined by subtracting the applied vertical load from the sum of the bolt load and the support reaction force. Fig. 14(b) plots the prying force evolutions in models H20-W120T10(15)(20)L230E25-12.9. It is observed that the thickness of the steel plate has limited influence on the development of prying force within the initial elastic stage.

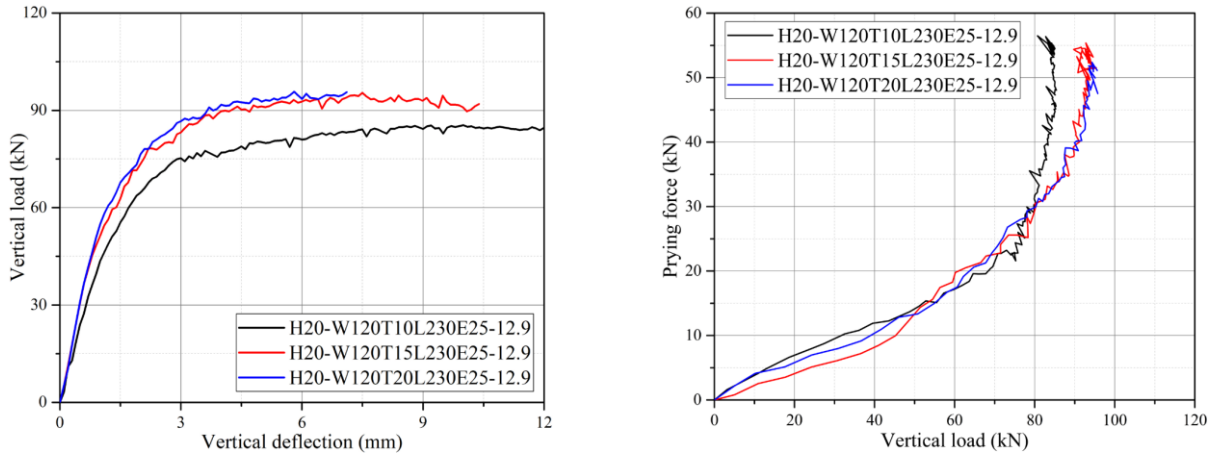

(a) (b)

Fig. 14. Load-deflection curves and prying force evolutions of models H20-W120T10(15)(20)L230E25-12.9 (a) load-deflection curves, (b) prying force evolutions.

3.2. Steel plate width

Increasing the width of the steel plate expanded the contact area between steel and concrete, thereby resulting in the reduced contact stress at the joint surface. As shown in Fig. 15, after increasing the width of the steel plate from 80 mm to 120 mm, localised concrete crushing found in the loaded block of the model H30-W80T20L230E15-12.9 was replaced by bolt fracture in the models H30-W100(120)T20L230E15-12.9. However, for models that fail by bolt fracture, the load-deflection curves plotted in Fig. 16 suggest that the width of the steel plate does not influence the deflection response of the connection system and the prying force evolution between the steel bar connection and plate.

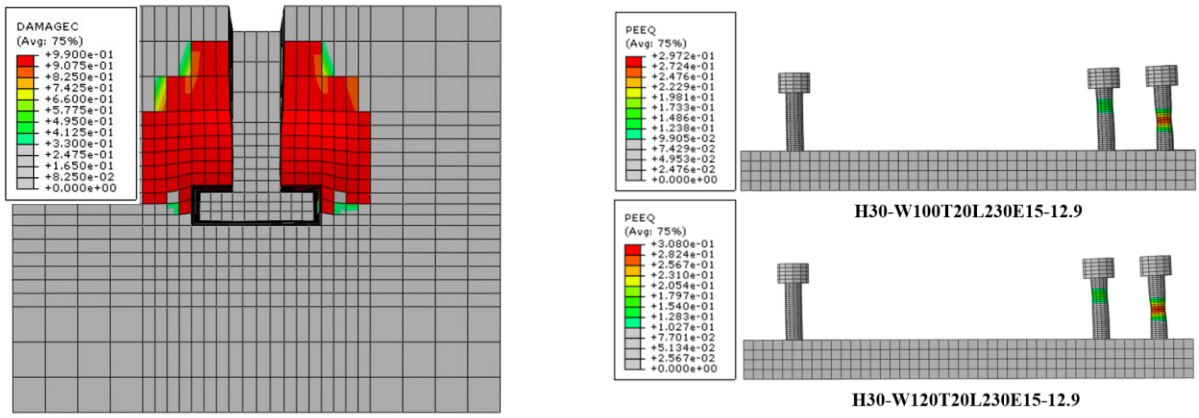

(a) (b)

Fig. 15. Failure modes of models H30-W80(100)(230)T20L230E15-12.9 (a) H30-W80T20L230E15-12.9-concrete crushing, (b) H30-W100(120)T20L230E15-12.9-bolt fracture.

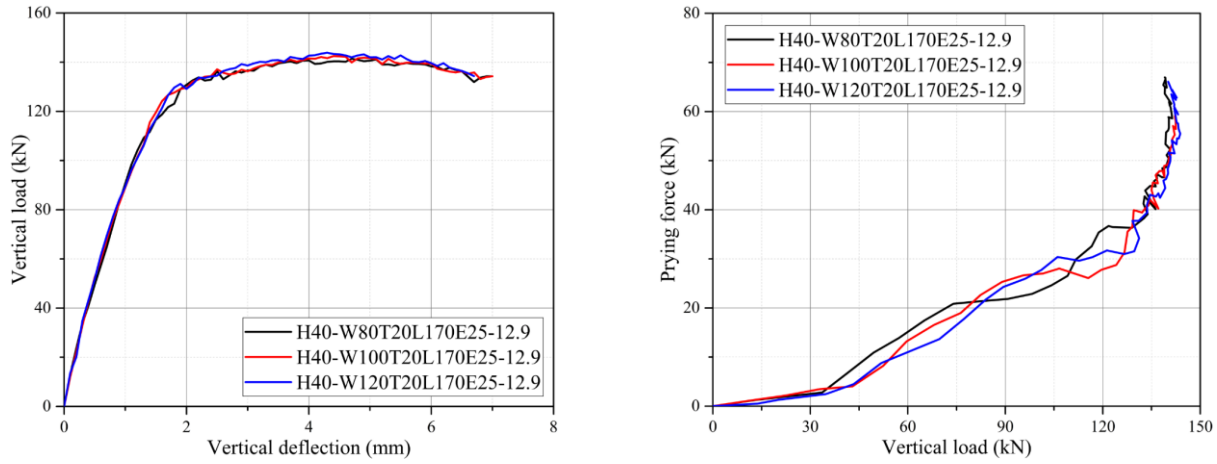

(a) (b)

Fig. 16. Load-deflection curves and prying force evolutions of models H40-W80(100)(120)T20L170E25-12.9 (a) load-deflection curves, (b) prying force evolutions.

3.3. Steel plate end distance

The end distance of the steel plate influenced the axial load development of high-strength bolts and the ultimate load of the proposed connection system. In the parametric analysis, the end distance between the first bolt and the joint surface was 15 mm (1.5*d*) or 25 mm (2.5*d*). Fig. 17(a) plots the generated load-deflection curves of models H30-W120T20L230E15(25)-12.9, respectively. It is found that reducing the steel plate end distance improves both the ultimate load and initial stiffness of models with the demountable connection system. As the steel plate end distance increased, an additional flexural deformation was created in the steel bar connection. Therefore, as shown in Fig. 17(b) and (c), the axial force development of the second bolt was restricted and the evolution of the prying force created between the steel bar connection and plate was accelerated. Fig. 18 describes the failure modes and load-deflection curves of the models H30-W100T15L230E15(25)-12.9. Despite the increased initial stiffness, reducing the end distance of the steel plate might lead to severe concrete crushing at the joint surface and result in a reduction in the ultimate load of the demountable connection system.

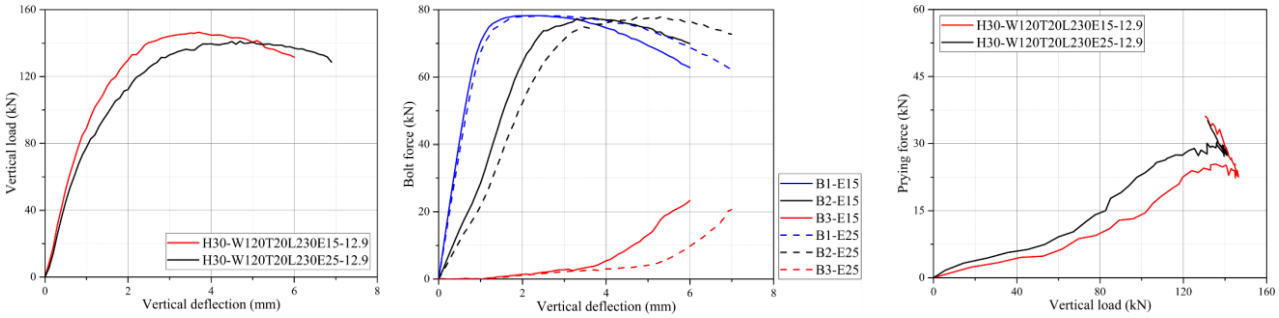

(a) (b) (c)

Fig. 17. Load-deflection curves, bolt force developments and prying force evolutions of models H30-W120T20L230E15(25)-12.9 (a) deflection responses, (b) bolt force developments, (c) prying force evolutions.

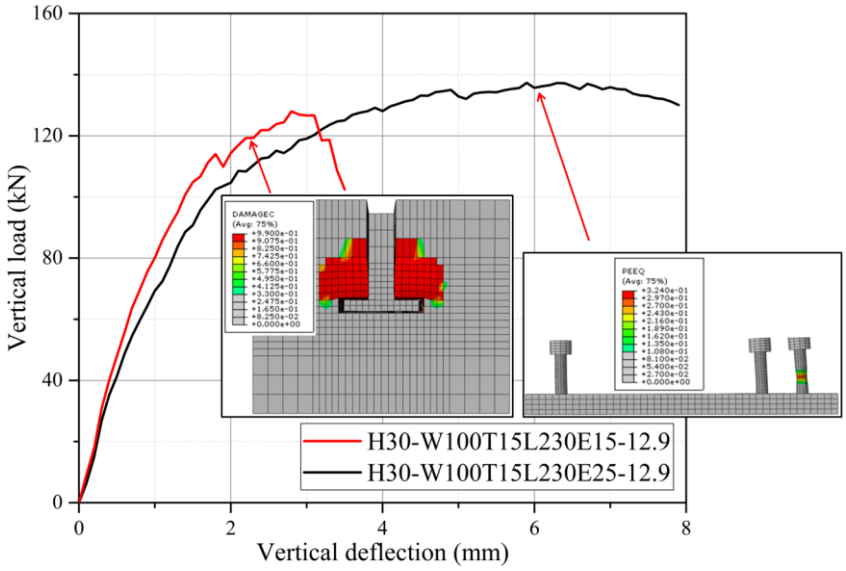

(a)

Fig. 18. Failure modes and load-deflection curves of models H30-W100T15L230E15(25)-12.9.

3.4. Steel plate length

To improve the structural performance of the demountable connection system and optimise the use of materials, steel plates with lengths of 110 mm, 170 mm and 230 mm were studied. For the model H40-W80T15L110E25-12.9, because of a limited contact area between steel and concrete, high compressive stress was created at the joint surface of the loaded block and led to severe concrete crushing as shown in Fig. 19(a). However, after increasing the steel plate length to 170 mm or 230 mm, the contact area between steel and concrete was expanded, which led to bolt fracture failure in the loaded block as found in Fig. 19(b). In addition, the length of the steel plate also affected the deflection response of models failed by bolt fracture. From the load-deflection curves plotted in Fig. 20(a), the model H40-

W120T20L110E25-12.9 exhibited the lowest initial stiffness compared with models equipped with 170 mm or 230 mm long steel plates. Fig. 20(b) plots the evolutions of prying force in these models, which indicates that the induced prying force increases as the length of the steel plate reduces. Under the same vertical load, high-strength bolts in the model H40-W120T20L110E25-12.9 were subjected to higher axial loads to take this increased prying force. Fig. 21 plots the developments of bolt load in models H40-W120T20L110(170)(230)E25-12.9. Because the third bolt in the model H40-W120T20L110-E25 experienced a rapid axial load development, the model H40-W120T20L110E25-12.9 could sustain a comparable ultimate load as other models despite being subjected to the highest prying force.

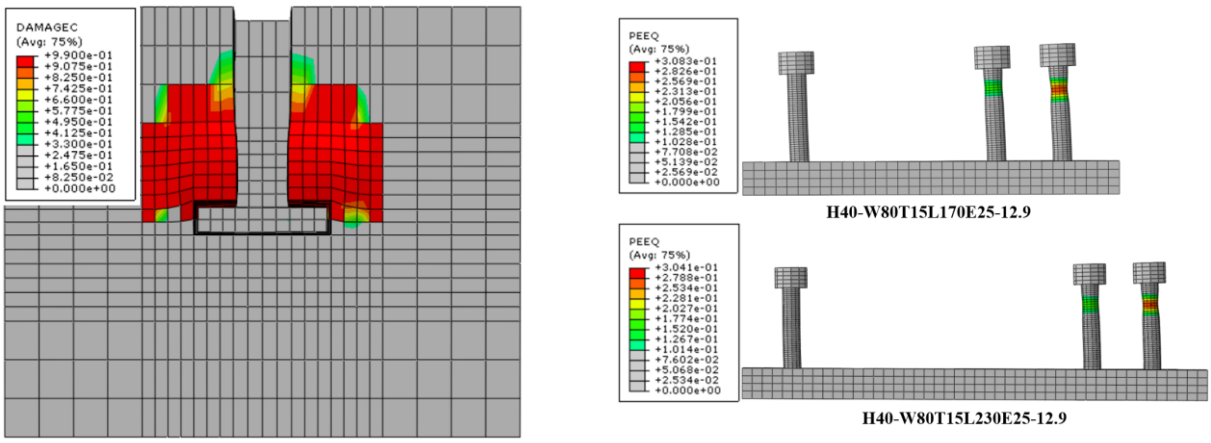

(a) (b)

Fig. 19. Failure modes of models H40-W80T15L110(170)(230)E25-12.9 (a) H40-W80T15L110E25-12.9, (b) H40-W80T15L170(230)E25-12.9.

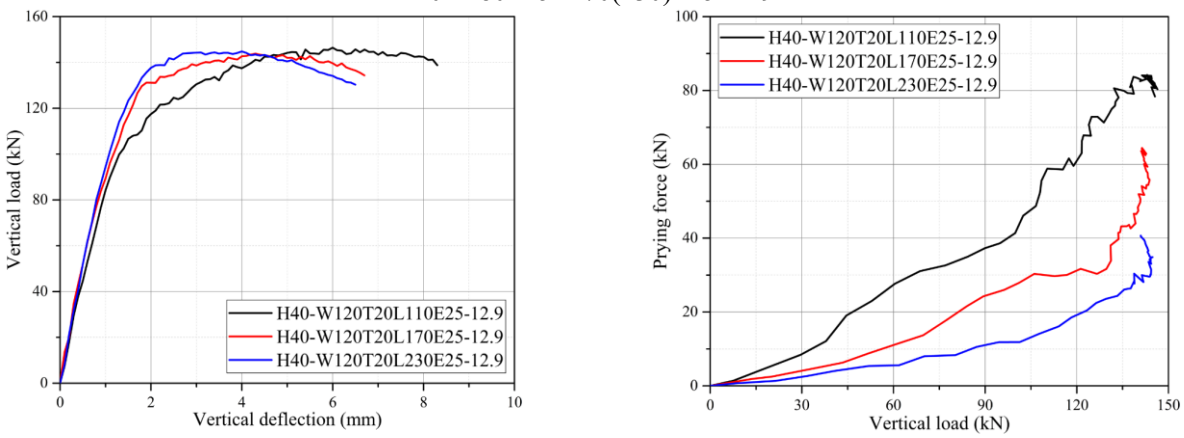

(a) (b)

Fig. 20. Load-deflection curves and prying force evolutions of models H40-W120T20L110(170)(230)E25-12.9 (a) load-deflection curves, (b) prying force evolutions.

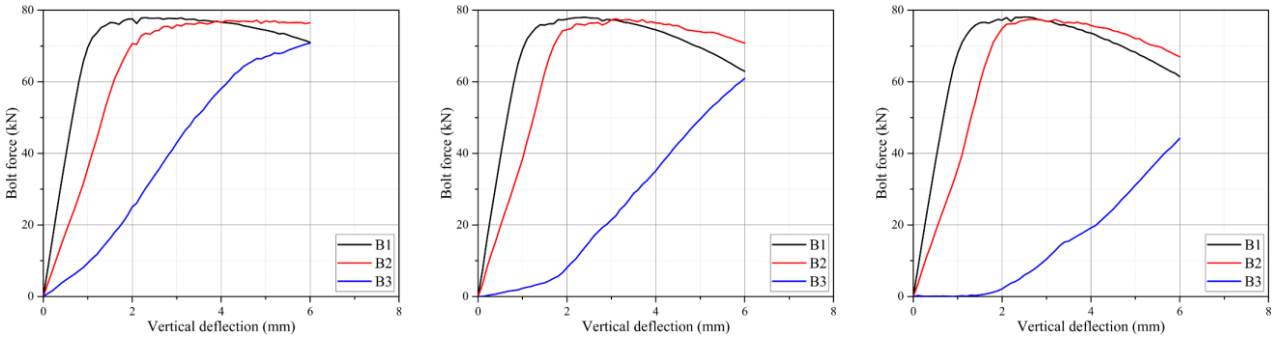

(a) (b) (c)

Fig. 21. Bolt forces developments of models H40-W120T20L110(170)(230)E25-12.9 (a) H40-W120T20L110E25-12.9, (b) H40-W120T20L170E25-12.9, (c) H40-W120T20L230E25-12.9

3.5. Steel bar connection height

In the parametric analysis, steel bar connections with a height of 10 mm (1*d*) to 40 mm (4*d*) were adopted. Under vertical load, the relative deformation between the steel bar connection and plate expanded as the height of the connection increased. As a result, as shown in Fig. 22, high-strength bolts in the model H40-W100T15L230E25-12.9 were subjected to the greatest axial forces, thereby resulting in an increased ultimate load and initial stiffness as verified in Fig. 23. The height of the steel bar connection also affected the evolution of prying force between contacted steel components. Under the same vertical load, the contact area between the steel bar connection and plate reduced as the height of the connection increased. Therefore, the evolution of the induced prying force was effectively lowered as plotted in Fig. 24. In addition, the failure mode of models with the demountable connection system was also influenced by the height of the steel bar connection. For the model H20-W100T15L230E15-12.9, the loaded block failed due to bolt fracture as the vertical load increased as shown in Fig. 25. However, as the connection height increased, the enhanced ultimate load resulted in high compressive stress of concrete and then led to localised concrete crushing at the joint surface.

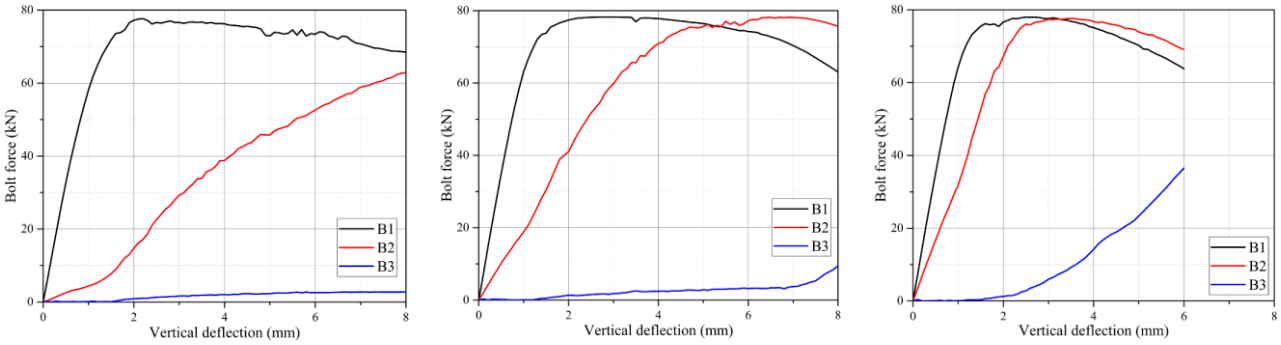

(a) (b) (c)

Fig. 22. Bolt force developments of models H20(30)(40)-W100T15L230E25-12.9 (a) H20-W100T15L230E25-12.9, (b) H30-W100T15L230E25-12.9, (c) H40-W100T15L230E25-12.9.

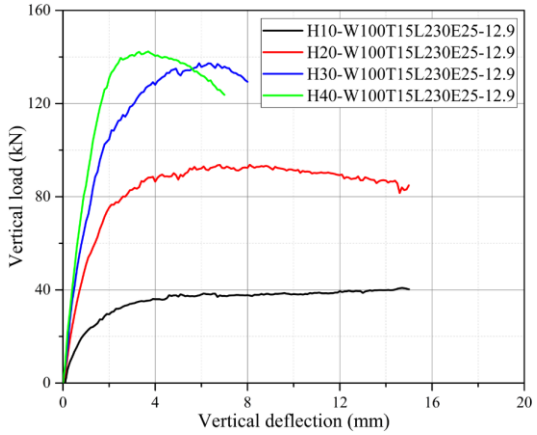

Fig. 23. Load-deflection curves of models H10(20)(30)(40)-W100T15L230E25-12.9.

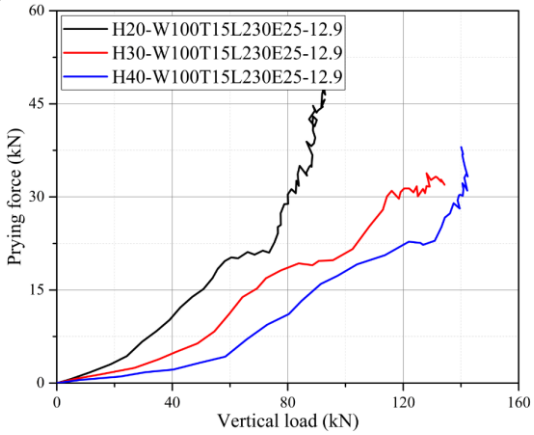

Fig. 24. Prying force evolutions of models H20(30)(40)-W100T15L230E25-12.9.

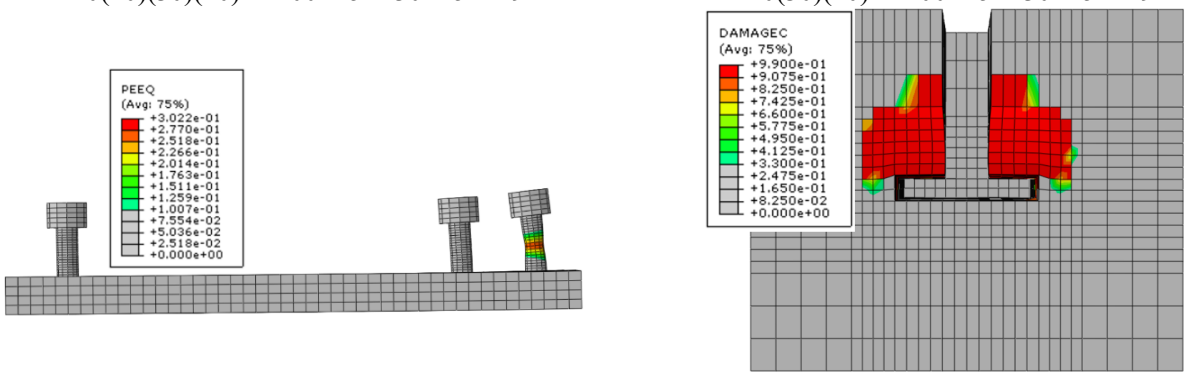

(a) (b)

Fig. 25. Failure modes of models H20(30)(40)-W100T15L230E15-12.9 (a) H20-W100T15L230E15-12.9-bolt fracture, (b) H30-W100T15L230E15-12.9-concrete crushing.

3.6. Bolt grade

Apart from 12.9 grade high-strength bolts, both 8.8 and 10.9 grade bolts were also investigated in the parametric analysis. Fig. 26 compares the failure modes of models H30-W100T15L110E15-12.9(10.9). Due to the superior tensile resistance of 12.9 grade high-strength bolts, brittle concrete crushing failure happened in the model H30-W100T15L110E15-12.9 before bolt fracture that was observed in the

335 model with 10.9 grade bolts. In terms of the deflection response, Fig. 27(a) plots the load-deflection
336 curves of models with different high-strength bolts. It is found that bolt grade is a key parameter that
337 influences the ultimate load of models with the demountable connection system. As the moduli of
338 elasticity of high-strength bolts were almost identical, each model exhibited similar initial stiffness as
339 the vertical load increased. Similarly, the effect of bolt grade on the prying force evolution in the initial
340 elastic stage was also negligible as depicted in Fig. 27(b).

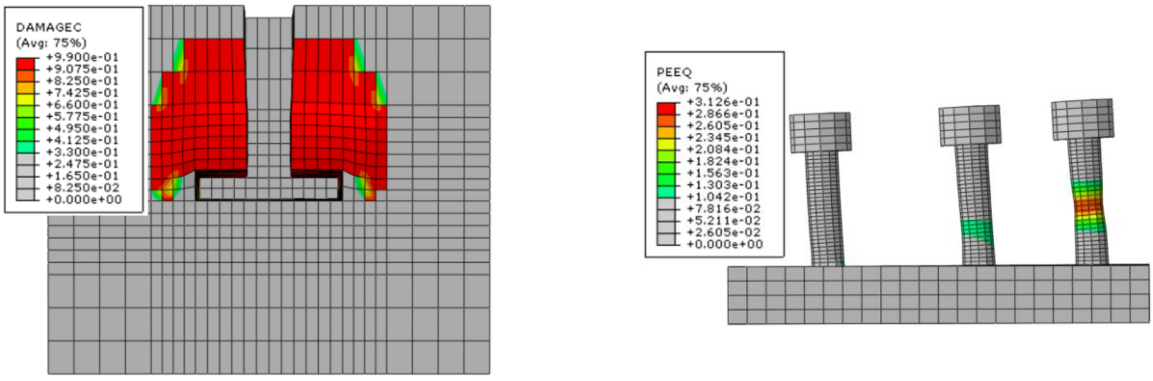

(a) (b)

Fig. 26. Failure modes of models H30-W100T15L110E15-12.9(10.9) (a) H30-W100T15L110E15-12.9-concrete crushing, (b) H30-W100T15L110E15-10.9-bolt fracture.

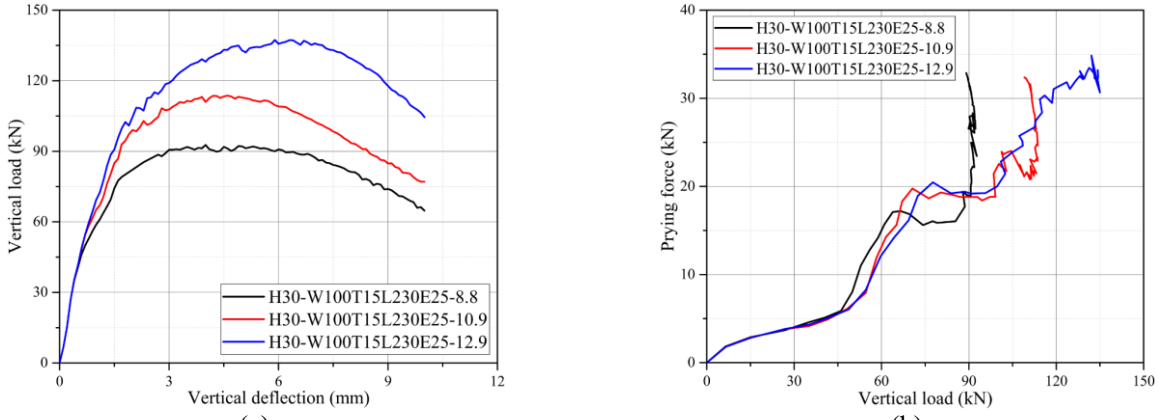

(a) (b)

Fig. 27. Load-deflection curves and prying forces evolutions of models H30-W100T15L230E25-12.9(10.9)(8.8) (a) load-deflection curves, (b) prying forces evolutions.

341 **4. Assessment of parameters**

342 Through the comprehensive parametric analysis, the effects of the steel plate thickness, width, end
343 distance, length, the steel bar connection height and high-strength bolt grade on the prying force
344 evolution between the steel plate and connection, the failure mode and the ultimate load of models with

345 the demountable connection system were studied. In contrast to the localised concrete crushing in the
346 loaded block, bolt fracture failure was preferred because high-strength bolts were commercially
347 available and replaceable. The ultimate load of models that failed due to bolt fracture was primarily
348 affected by the end distance of the steel plate, the height of the steel bar connection and high-strength
349 bolt grade. Among these parameters, the steel bar connection height and the steel plate end distance
350 also influenced the initial stiffness of models employing the demountable connection system. The
351 prying force between the steel plate and connection reduced by increasing the connection height and
352 reducing the plate end distance. As the length of the steel plate had little influence on the ultimate load
353 and initial stiffness of developed models, it could be optimised to 110 mm to achieve a reliable
354 structural performance with low material costs.

355 **5. Design load prediction**

356 The main objective of proposing the demountable steel connection system was to achieve the flexible
357 installation and disassembly of PCP units. Therefore, to prevent the necking of bolt shank that might
358 hinder the disassembly process, the design load of the connection system was defined as the transferred
359 vertical load when the first bolt reached the ultimate load as introduced in Fig. 28, where F_d is the
360 design load of the connection system; B1, B2 and B3 are axial loads developed in high-strength bolts,
361 respectively. Following this definition, three typical failure mechanisms were observed in the
362 parametric analysis as shown in Fig. 29.

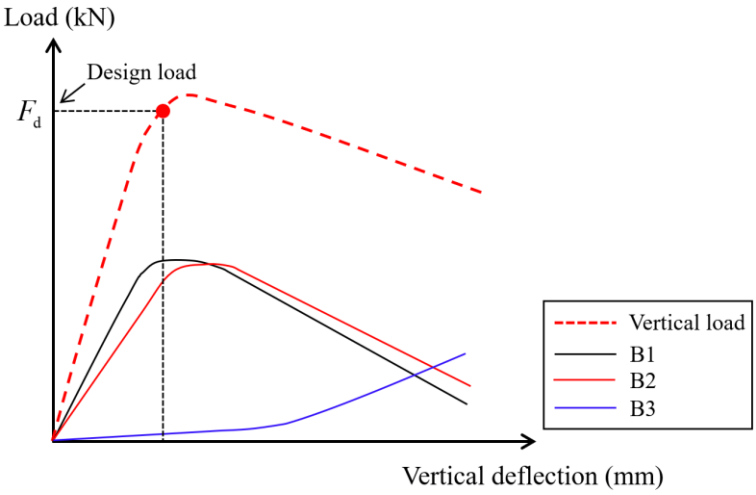

Fig. 28. Defination of design load F_d.

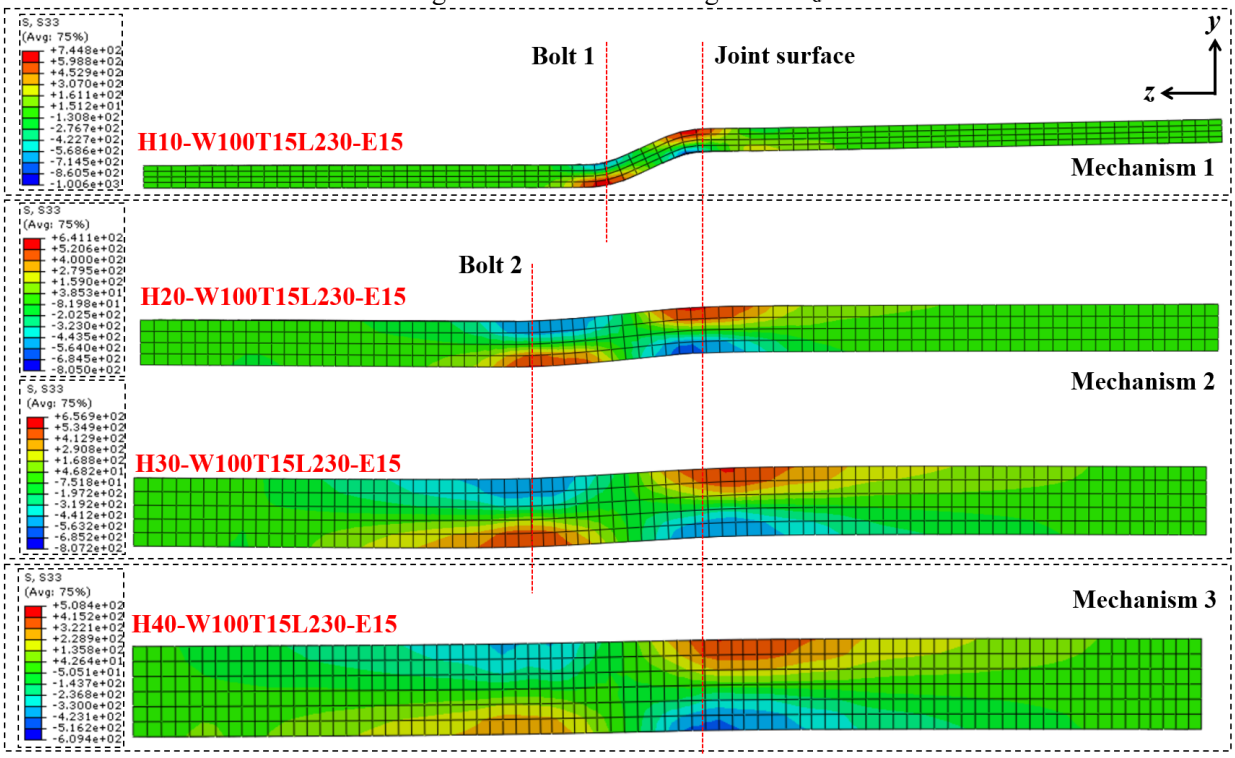

Fig. 29. Failure mechanisms observed in parametric analysis.

5.1. Failure mechanism 1

The failure mechanism 1 was the formation of two plastic hinges in the steel bar connection at the first high-strength bolt and at the joint surface of the reaction block, respectively. Since no bolt fracture failure happened as the vertical load increased, the steel bar connection experienced a large flexural deformation, from which the strain hardening characteristic of stainless steel was fully developed. Fig. 30 describes the failure mechanism 1 and the analytical model of this mechanism is established based

on the corresponding moment equilibrium as expressed by Eqs. (18) to (20), where w_s and h_s refer to the width and height of the steel bar connection, m is the distance between the first bolt and the joint surface of the reaction block, M_u denotes the ultimate moment resistance of the steel bar connection, F_d is the design load transferred by the steel bar connection.

$$M_u = \frac{1}{4} w_s h_s^2 f_u \tag{18}$$

$$F_d m = 2M_u \tag{19}$$

$$F_d = \frac{2M_u}{m} = \frac{w_s h_s^2 f_u}{2m} \tag{20}$$

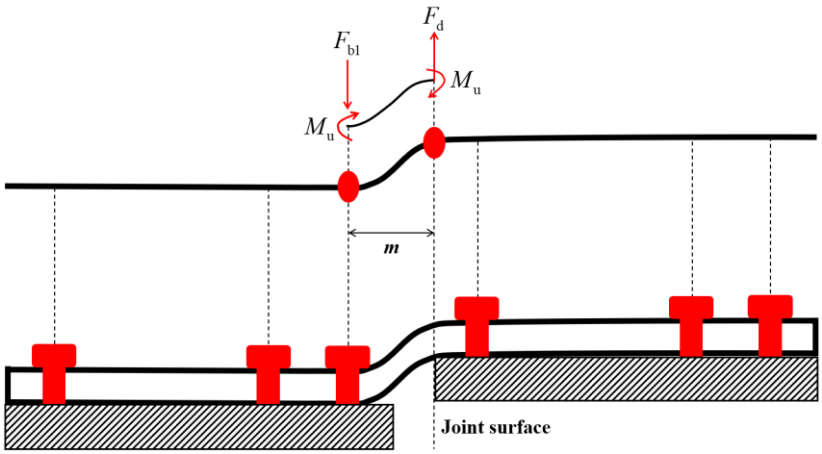

Fig. 30. Failure mechanism 1.

Under vertical load, the free body diagrams of the steel bar connection and the concrete block with the embedded plate are shown in Fig. 31, from which the corresponding force equilibriums are derived as expressed by Eqs. (21) and (22), where, F_v is the applied vertical load; F_{b1}, F_{b2} and F_{b3} refer to the developed bolt loads in the high-strength bolts B1, B2 and B3, respectively; F_s and F_p are the support reaction force and the prying force, respectively; F_t denotes the shear force transferred by the steel connection; M is the moment of the steel bar connection at the joint surface of the reaction block. After computing the transferred load by acquiring the applied vertical load, bolt loads and the support reaction force from FEA, Table 6 compares the design loads predicted by the analytical solution and

384 generated in FEA. The accuracy of the prediction is confirmed by the mean value of 1.00 and the

385 coefficient of variation (CoV) of 0.03.

386 $$F_v = F_{b1} + F_{b2} + F_{b3} + F_s - F_p \quad (21)$$

387 $$F_t = F_{b1} + F_{b2} + F_{b3} - F_p \quad (22)$$

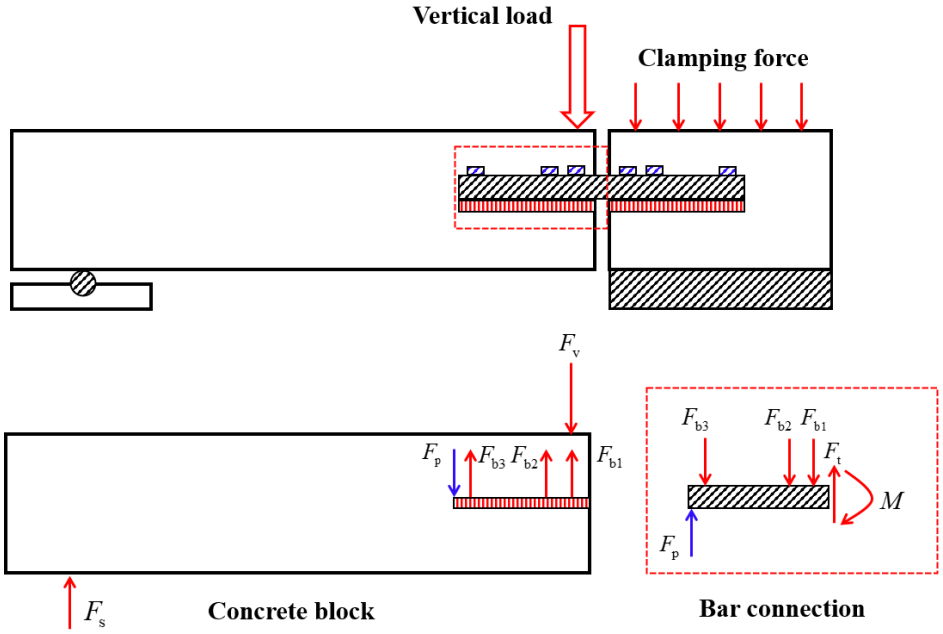

Fig. 31. Free body diagrams of concrete block and steel bar connection.

388 Table 6 Predicted design load (failure mechanism 1).

Model ID	M_u (kN·m)	$F_{d,pred}$ (kN)	$F_{d,FE}$ (kN)	$F_{d,pred}/F_{d,FE}$
H10-W100T15L110E15-12.9	0.62	44.73	46.70	0.96
H10-W100T15L110E25-12.9	0.62	32.80	33.32	0.98
H10-W100T15L170E15-12.9	0.62	44.73	46.85	0.95
H10-W100T15L170E25-12.9	0.62	32.80	33.41	0.98
H10-W100T15L230E15-12.9	0.62	44.73	46.54	0.96
H10-W100T15L230E25-12.9	0.62	32.80	33.40	0.98
H10-W100T15L110E25-8.8	0.62	32.80	32.62	1.01
H10-W100T15L170E25-8.8	0.62	32.80	32.63	1.01
H10-W100T15L230E25-8.8	0.62	32.80	32.66	1.00
H10-W100T15L110E15-10.9	0.62	44.73	43.30	1.03
H10-W100T15L110E25-10.9	0.62	32.80	33.39	0.98
H10-W100T15L170E15-10.9	0.62	44.73	42.76	1.05
H10-W100T15L170E25-10.9	0.62	32.80	33.31	0.98
H10-W100T15L230E15-10.9	0.62	44.73	43.04	1.04
H10-W100T15L230E25-10.9	0.62	32.80	33.52	0.98
			Average	1.00
			CoV	0.03

389 **5.2. Failure mechanism 2**

390 Failure mechanism 2 happened in the models with a steel bar connection of 20 mm or 30 mm heights.

When the first bolt reached the ultimate load, as displayed in Fig. 32, two plastic hinges formed in the steel bar connection at the locations of the second bolt and the joint surface of the reaction block, respectively. The moment equilibrium about the plastic hinge at the second bolt are expressed by Eqs. (23) to (25), where e_1 is the spacing between the first bolt and the second bolt equal to 30 mm ($3d$); A_0 represents the net section area of high-strength bolts; M_{pl} is the plastic moment resistance of the steel bar connection. As the strain hardening behaviour of stainless steel was not completely developed when the first bolt reached the ultimate load, the plastic moment resistance M_{pl} was determined by the yield strength of the connection as indicated in Eq. (26). Table 7 summarises the design loads generated from the FEA data and computed by the analytical approach. Close agreements are achieved with the mean value of 1.01 and the coefficient of variation (CoV) of 0.04.

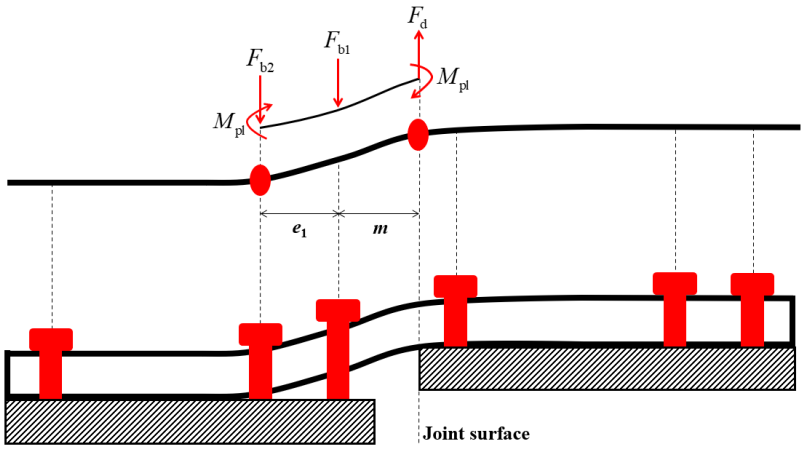

Fig. 32. Failure mechanism 2.

$$F_d(m+e_1) = F_{b1}e_1 + 2M_{pl} \tag{23}$$

$$F_{b1} = f_{ub}A_0 \tag{24}$$

$$F_d = \frac{f_{ub}A_0e_1 + 2M_{pl}}{m+e_1} \tag{25}$$

$$M_{pl} = \frac{1}{4}w_s h_s^2 f_y \tag{26}$$

Table 7 Predicted design load (failure mechanism 2).

Model ID	M_{pl} (kN·m)	$F_{d,pred}$ (kN)	$F_{d,FE}$ (kN)	$F_{d,pred}/F_{d,FE}$

H20-W80T15L110E25-12.9	1.18	71.35	72.59	0.98
H20-W80T15L170E25-12.9	1.18	71.35	73.45	0.97
H20-W80T15L230E25-12.9	1.18	71.35	73.59	0.97
H20-W80T20L110E25-12.9	1.18	71.35	72.55	0.98
H20-W80T20L170E25-12.9	1.18	71.35	72.57	0.98
H20-W80T20L230E25-12.9	1.18	71.35	71.65	1.00
H30-W80T15L170E25-12.9	2.66	115.13	110.47	1.04
H30-W80T15L230E25-12.9	2.66	115.13	110.53	1.04
H30-W80T20L110E25-12.9	2.66	115.13	108.51	1.06
H30-W80T20L170E25-12.9	2.66	115.13	110.83	1.04
H30-W80T20L230E25-12.9	2.66	115.13	110.7	1.04
H20-W100T15L110E25-12.9	1.18	71.35	72.52	0.98
H20-W100T15L170E15-12.9	1.18	83.76	83.55	1.00
H20-W100T15L170E25-12.9	1.18	71.35	73.58	0.97
H20-W100T15L230E15-12.9	1.18	83.76	82.45	1.02
H20-W100T15L230E25-12.9	1.18	71.35	70.66	1.01
H20-W100T20L110E15-12.9	1.18	83.76	85.8	0.98
H20-W100T20L110E25-12.9	1.18	71.35	72.63	0.98
H20-W100T20L170E15-12.9	1.18	83.76	83.11	1.01
H20-W100T20L170E25-12.9	1.18	71.35	73.43	0.97
H20-W100T20L230E15-12.9	1.18	83.76	83.61	1.00
H20-W100T20L230E25-12.9	1.18	71.35	74.92	0.95
H30-W100T15L110E25-12.9	2.66	115.13	106.07	1.09
H30-W100T15L170E25-12.9	2.66	115.13	108.07	1.07
H30-W100T15L230E25-12.9	2.66	115.13	108.88	1.06
H30-W100T20L170E15-12.9	2.66	135.15	127.74	1.06
H30-W100T20L170E25-12.9	2.66	115.13	110.72	1.04
H30-W100T20L230E15-12.9	2.66	135.15	128.01	1.06
H30-W100T20L230E25-12.9	2.66	115.13	116.95	0.98
H20-W120T10L170E25-12.9	1.18	71.35	72.82	0.98
H20-W120T10L230E25-12.9	1.18	71.35	72.6	0.98
H20-W120T15L110E15-12.9	1.18	83.76	81.39	1.03
H20-W120T15L110E25-12.9	1.18	71.35	74.07	0.96
H20-W120T15L170E15-12.9	1.18	83.76	85.41	0.98
H20-W120T15L170E25-12.9	1.18	71.35	71.25	1.00
H20-W120T15L230E15-12.9	1.18	83.76	84.69	0.99
H20-W120T15L230E25-12.9	1.18	71.35	71.65	1.00
H20-W120T20L110E15-12.9	1.18	83.76	87.9	0.95
H20-W120T20L110E25-12.9	1.18	71.35	75.66	0.94
H20-W120T20L170E15-12.9	1.18	83.76	86.25	0.97
H20-W120T20L170E25-12.9	1.18	71.35	74.09	0.96
H20-W120T20L230E15-12.9	1.18	83.76	83.32	1.01
H20-W120T20L230E25-12.9	1.18	71.35	73.77	0.97
H30-W120T15L110E25-12.9	2.66	115.13	106.01	1.09
H30-W120T15L170E25-12.9	2.66	115.13	111.74	1.03
H30-W120T15L230E25-12.9	2.66	115.13	110.96	1.04
H30-W120T20L110E25-12.9	2.66	115.13	111.02	1.04
H30-W120T20L170E15-12.9	2.66	135.15	126.81	1.07
H30-W120T20L170E25-12.9	2.66	115.13	116.02	0.99
H30-W120T20L230E15-12.9	2.66	135.15	127.61	1.06
H30-W120T20L230E25-12.9	2.66	115.13	115.28	1.00
H30-W100T15L110E25-10.9	2.66	107.24	97.79	1.10
H30-W100T15L170E25-10.9	2.66	107.24	100.04	1.07
H30-W100T15L230E25-10.9	2.66	107.24	102.53	1.05
			Average	1.01
			CoV	0.04

5.3. Failure mechanism 3

When the first high-strength bolt reached the ultimate load, models equipped with a steel bar connection of 30 mm or 40 mm height failed due to the failure mechanism 3, in which a plastic hinge developed at the joint surface of the reaction block as described in Fig. 33. Taking into account the assumption of rigid-plastic deformation for the steel bar connection, the axial deformation of high-strength bolts is proportional to the distance between the bolt position and the end of the connection. For high-strength bolts simplified by elastic components, the developed axial loads can be calculated by Eqs. (27) to (29), where e_2 is the spacing between the second and the third bolts; e_3 is the distance between the third bolt and the end of the steel bar connection. As a result, the moment equilibrium about the connection end is established as expressed by Eq. (30), from which the design load can be derived through Eq. (31). Table 8 compares the designed loads of models dominated by the failure mechanism 3. The slight difference of the design load prediction possibly comes from the overestimation of the bending moment of the steel bar connection at the joint surface of the reaction block. The high flexural stiffness of the steel bar connection makes the plastic hinge less developed under the design load.

$$F_{b1} = f_{ub} A_0 \tag{27}$$

$$F_{b2} = F_{b1}\left(\frac{e_2 + e_3}{e_1 + e_2 + e_3}\right) \tag{28}$$

$$F_{b3} = F_{b1}\left(\frac{e_3}{e_1 + e_2 + e_3}\right) \tag{29}$$

$$F_d(m + e_1 + e_2 + e_3) = M_{pl} + F_{b1}(e_1 + e_2 + e_3) + F_{b2}(e_2 + e_3) + F_{b3}e_3 \tag{30}$$

425

$$F_{\mathrm{d}}=\frac{M_{\mathrm{pl}}+f_{\mathrm{ub}}A_0\left[e_1+e_2+e_3+\dfrac{(e_2+e_3)^2}{e_1+e_2+e_3}+\dfrac{e_3^{\,2}}{e_1+e_2+e_3}\right]}{m+e_1+e_2+e_3} \tag{31}$$

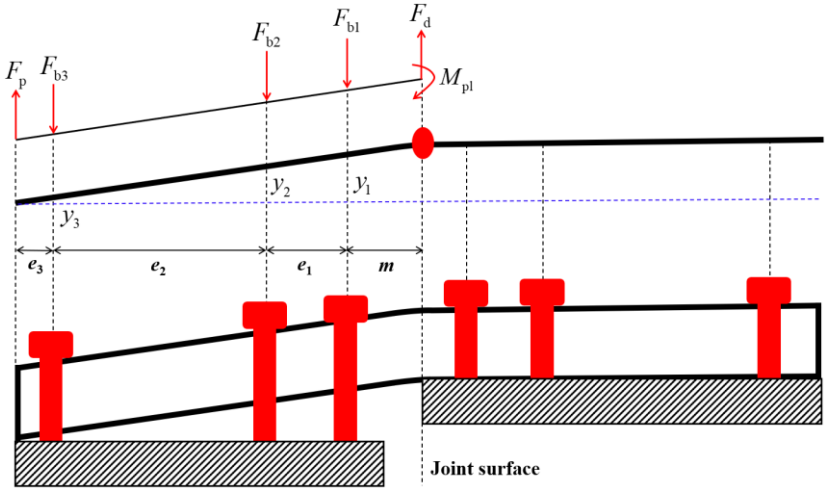

Fig. 33. Failure mechanism 3.

426 Table 8 Predicted design load (failure mechanism 3).

Model ID	M_{pl} (kN·m)	$F_{\mathrm{d,pred}}$ (kN)	$F_{\mathrm{d,FE}}$ (kN)	$F_{\mathrm{d,pred}}/F_{\mathrm{d,FE}}$
H40-W80T15L170E25-12.9	4.73	133.64	122.76	1.09
H40-W80T15L230E25-12.9	4.73	139.99	129.11	1.08
H40-W80T20L110E25-12.9	4.73	123.97	115.71	1.07
H40-W80T20L170E25-12.9	4.73	133.64	125.94	1.06
H40-W80T20L230E25-12.9	4.73	139.99	130.61	1.07
H40-W100T15L110E25-12.9	4.73	123.97	115.17	1.08
H40-W100T15L170E25-12.9	4.73	133.64	125.67	1.06
H40-W100T15L230E25-12.9	4.73	139.99	129.69	1.08
H40-W100T20L110E25-12.9	4.73	123.97	117.19	1.06
H40-W100T20L170E15-12.9	4.73	142.30	135.47	1.05
H40-W100T20L170E25-12.9	4.73	133.64	127.32	1.05
H40-W100T20L230E15-12.9	4.73	146.61	138.95	1.06
H40-W100T20L230E25-12.9	4.73	139.99	133.22	1.05
H40-W120T15L110E25-12.9	4.73	123.97	117.07	1.06
H40-W120T15L170E25-12.9	4.73	133.64	125.51	1.06
H40-W120T15L230E25-12.9	4.73	139.99	129.63	1.08
H40-W120T20L110E25-12.9	4.73	123.97	117.02	1.06
H40-W120T20L170E15-12.9	4.73	142.30	134.11	1.06
H40-W120T20L170E25-12.9	4.73	133.64	125.98	1.06
H40-W120T20L230E15-12.9	4.73	146.61	136.94	1.07
H40-W120T20L230E25-12.9	4.73	139.99	132.33	1.06
H30-W100T15L110E15-8.8	2.66	81.08	85.39	0.95
H30-W100T15L110E25-8.8	2.66	74.46	79.78	0.93
H30-W100T15L170E15-8.8	2.66	86.49	87.49	0.99
H30-W100T15L170E25-8.8	2.66	81.14	83.24	0.97
H30-W100T15L230E15-8.8	2.66	89.51	86.44	1.04
H30-W100T15L230E25-8.8	2.66	85.42	83.95	1.02
H30-W100T15L110E15-10.9	2.66	97.99	100.47	0.98
H30-W100T15L110E25-10.9	2.66	88.53	93.87	0.94
H30-W100T15L170E15-10.9	2.66	105.67	103.55	1.02
H30-W100T15L230E15-10.9	2.66	110.46	106.08	1.04
			Average	1.04
			CoV	0.04

6. Design recommendations

According to the parametric analysis results and the proposed analytical models, the following design recommendations can be drawn to instruct the design of the demountable steel connection system:

1. Compared with brittle concrete crushing failure in the loaded concrete block, bolt fracture is expected because high-strength bolts are available in the market and are easy to replace.
2. The thickness of the steel plate should be as least 15 mm to prevent localised concrete crushing in the loaded block.
3. Reducing the length of the steel bar connection does not impair the ultimate load of the demountable connection system. Therefore, the length of the steel plate can be minimised to reduce the material cost. By carrying out the parametric analysis, the steel plate with a length of 110 mm is suggested.
4. According to the derived analytical models, failure mechanism 1 is not expected because of a large flexural deformation created in the steel bar connection. The steel bar connection with a height of at least 20 mm is recommended to prevent this failure and improve the reusability of the proposed connection system.
5. The demountable steel connection system with high initial stiffness is suggested to reduce the relative deflection between pavement slabs under vertical load. Following this principle, the models H40-W100T15L110E25-12.9, H30-W100T15L110E15-10.9 and H30-W100T15L110E15-8.8 are recommended in terms of different grades of high-strength bolts.

7. Conclusions

In this paper, the structural performance of concrete blocks with the demountable steel connection

system under vertical load was investigated through FEA. After being validated against test results, a comprehensive parametric analysis was conducted to study the effects of the steel plate thickness, width, end distance, length, the steel bar connection height and high-strength bolt grade on the failure mode and ultimate load of the connection system, and the evolution of prying force between the steel bar connection and plate. The following conclusions are put forward on the basis of the obtained FEA results:

1. For models that fail due to bolt fracture, the width of the steel plate has little influence on the structural performance of models with the demountable steel connection system.
2. Reducing the steel plate end distance and increasing the height of the steel bar connection can effectively improve the ultimate load and initial stiffness of the demountable steel connection system.
3. Increasing the grade of high-strength bolts significantly enhances the ultimate load of the models that fail due to bolt fracture. However, the initial stiffness of these models is almost the same for different bolt grades.
4. The evolution of prying force between the steel bar connection and plate reduces with the increase of the height and length of the steel bar connection, while accelerates as the steel plate end distance increases.
5. To prevent the necking of high-strength bolts, the design load of the demountable steel connection system is specified when the first bolt reaches its ultimate load. According to three failure mechanisms observed in the parametric analysis, the corresponding analytical models are proposed to predict the design load of the connection system.

Acknowledgements

The research work presented in this paper was supported by a grant from the Research Grants Council of the Hong Kong Special Administrative Region, China (Project no. R5007-18). Authors would like to sincerely acknowledge the advice on the joint design from Professor Yuhong Wang at The Hong Kong Polytechnic University.

References

[1]. Tayabji S, Ye D, Buch N. Precast Concrete Pavement Technology. Washington, DC: Transportation Research Board 2013.

[2]. Tayabji S, Ye D, Buch N. Precast concrete pavements: Technology overview and technical considerations. PCI journal 2013;58,112-128.

[3]. Vaitkus A, Šernas O, Gražulytė J. Modular pavements: Developing high performance concrete. Construction Building Materials 2021;292:123362.

[4]. Tomek R. Advantages of precast concrete in highway infrastructure construction. Procedia engineering 2017;196:176-180.

[5]. Guo J-C, Chan T-M, Wang Y-H. Experimental investigation on the structural performance of the high-strength ring strengthened dowel connection under monotonic load. Engineering Structures 2023;292:116423.

[6]. Novak J, Kohoutková A, Křístek V, Vodička J. Precast concrete pavement–systems and performance review. IOP Conference Series: Materials Science and Engineering 2017. 012030.

[7]. Smith P, Snyder MB. Manual for Jointed Precast Concrete Pavement, National Precast Concrete Association 2019.

[8]. Cookson G. Europes Traffic Hotspots Measuring the impact of congestion. INRIX research 2016.

[9]. Syed A, Sonparote R. A Review of Precast Concrete Pavement Technology. Baltic Journal of Road Bridge Engineering 2020;15:22-53.

[10]. Fang MJ, Zhou R, Ke WH, Tian B, Zhang YB, Liu JJ. Precast system and assembly connection of cement concrete slabs for road pavement: A review. Journal of Traffic and Transportation Engineering-English Edition 2022;9:208-222.

[11]. Vaitkus A, Gražulytė J, Kleizienė R, Vorobjovas V, Šernas O. Concrete modular pavements–types, issues and challenges. The Baltic Journal of Road Bridge Engineering 2019;14:80-103.

[12]. Gopalaratnam VS, Donahue J, Davis B, Dailey C. Precast Prestressed Panels for Rapid Full-Depth Pavement Repairs. Structures Congress 2006: Structural Engineering and Public Safety 2006;1-10.

[13]. DoT, U.S., FHWA, F. Status of the Nation's Highways, Bridges, and Transit: Conditions and Performance. Report to Congress 2006.

[14]. Merritt DK, McCullough BF, Burns NH. Texas Tests Precast for Speed and Usability. Public Roads 2002;66:30-34.

509 [15]. Merritt DK, Tayabji S, Precast Prestressed Concrete Pavement for Reconstruction and
510 Rehabilitation of Existing Pavements. 2009

511 [16]. Priddy LP, Bly PG, Flintsch GW. Review of precast portland cement concrete panel
512 technologies for use in expedient portland cement concrete airfield pavement repairs.
513 2013.

514 [17]. Offenbacker D, Cleary D, Ali A, Mehta Y. Developing specifications for precast concrete
515 highway pavements. International Journal of Pavement Engineering 2022;23:1791-1799.

516 [18]. De Larrard F, Sedran T, Balay J-M. Removable urban pavements: an innovative,
517 sustainable technology. International Journal of Pavement Engineering 2013;14:1-11.

518 [19]. Syed A, Sonparote RS. Construction of Pretensioned Precast Concrete Pavement. Iranian
519 Journal of Science and Technology-Transactions of Civil Engineering 2020;44:507-514.

520 [20]. Tayabji S, Ye D, Buch N. Joint Load Transfer and Support Considerations for Jointed
521 Precast Concrete Pavements. Transportation Research Record 2012;2305:74-80.

522 [21]. Priddy LP, Bly PG, Jackson CJ, Flintsch GW. Full-scale field testing of precast Portland
523 cement concrete panel airfield pavement repairs. International Journal of Pavement
524 Engineering 2014;15:840-853.

525 [22]. Li H. Evaluation of jointed plain concrete pavement (JPCP) with FRP dowels. 2004.

526 [23]. Eddie D, Shalaby A, Rizkalla S. Glass fiber-reinforced polymer dowels for concrete
527 pavements. ACI Structural Journal 2001;98:201-206.

528 [24]. Benmokrane B, Ahmed EA, Montaigu M, Thebeau D. Performance of Glass Fiber-
529 Reinforced Polymer-Doweled Jointed Plain Concrete Pavement under Static and Cyclic
530 Loadings. ACI Structural Journal 2014;111:331-341.

531 [25]. Khazanovich L, Yut I, Tompkins D, Schultz A. Accelerated loading testing of stainless
532 steel hollow tube dowels. Transportation research record 2006;1947:101-109.

533 [26]. Guo J-C, Chan T-M. Experimental and numerical study on the structural performance of
534 the stainless steel ring strengthened removable dowel bar connection system.
535 International Journal of Pavement Engineering 2022; 1-24.

536 [27]. Guo J-C, Chan T-M. Stainless steel ring strengthened removable dowel bar connection
537 system: Effect of key parameters and design recommendations. Structures 2022;44:1767-
538 1782.

539 [28]. Zaman M, Alvappillai A. Contact-element model for dynamic analysis of jointed
540 concrete pavements. Journal of Transportation Engineering 1995;121:425-433.

541 [29]. Huang Y, Wang S. Finite-element analysis of concrete slabs and its implications for rigid
542 pavement design. Highway Research Record 1973.

543 [30]. Huang Y. A computer package for structural analysis of concrete pavements. Third

544 International Conference on Concrete Pavement Design and Rehabilitation, Purdue
545 University 1985.

546 [31]. Mahboub KC, Liu Y, Allen DL. Evaluation of temperature responses in concrete
547 pavement. Journal of Transportation Engineering 2004;130:395-401.

548 [32]. Guo H, Sherwood JA, Snyder MB. Component dowel-bar model for load-transfer
549 systems in PCC pavements. Journal of Transportation Engineering 1995;121:289-298.

550 [33]. Tayabji SD, Colley BE. Analysis of jointed concrete pavements. 1986.

551 [34]. Tabatabaie AM, Barenberg E. Finite-element analysis of jointed or cracked concrete
552 pavements. Transportation Research Record 1978;11-19.

553 [35]. Tia M, Armaghani JM, Wu C-L, Lei S, Toye KL. FEACONS III computer program for
554 analysis of jointed concrete pavements. Transportation Research Record 1987.

555 [36]. Bhattacharya K. Nonlinear response of transverse joints of airfield pavements. Journal of
556 Transportation Engineering 2000;126:168-177.

557 [37]. Channakeshava C, Barzegar F, Voyiadjis GZ. Nonlinear FE analysis of plain concrete
558 pavements with doweled joints. Journal of Transportation Engineering 1993;119:763-
559 781.

560 [38]. Kim J, Hjelmstad KD. Three-dimensional finite element analysis of doweled joints for
561 airport pavements. Transportation Research Record 2003;1853:100-109.

562 [39]. Maitra SR, Reddy K, Ramachandra L. Load transfer characteristics of dowel bar system
563 in jointed concrete pavement. International Journal of Fracture 2009;135:813-821.

564 [40]. Al-Humeidawi BH, Mandal P. Evaluation of performance and design of GFRP dowels in
565 jointed plain concrete pavement–part 2: numerical simulation and design considerations.
566 International Journal of Pavement Engineering 2014;15:752-765.

567 [41]. Mackiewicz P. Finite-element analysis of stress concentration around dowel bars in
568 jointed plain concrete pavement. Journal of Transportation Engineering
569 2015;141(6):06015001.

570 [42]. Priddy LP, Doyle JD, Flintsch GW, Pittman DW, Anderton GL. Three-dimensional
571 modelling of precast concrete pavement repair joints. Magazine of Concrete Research
572 2015;67:513-522.

573 [43]. Mackiewicz P, Szydło A. The analysis of stress concentration around dowel bars in
574 concrete pavement. Magazine of Concrete Research 2020;72:97-107.

575 [44]. Al-Humeidawi BH, Mandal P. Numerical evaluation of the combined effect of dowel
576 misalignment and wheel load on dowel bars performance in JPCP. Engineering
577 Structures 2022;252:113655.

578 [45]. Guo J-C, Chan T-M. Characteristics of compressive stress around dowel joint in concrete

pavement system. International Journal of Pavement Engineering 2022;1-17.

[46]. Guo J-C, Chan T-M, Wang Y-H. Test, modelling and design of a demountable stainless steel bar connection system for precast concrete pavements. Engineering Structures 2023;301:117231.

[47]. AASHTO T253: Standard Method of Test for Coated Dowel Bars 2011.

[48]. AASHTO guide for design of pavement structure. Washington D.C: American Association of State Highway and Transportation Officials 1993.

[49]. ABAQUS 6.14, Dassault Systems, Waltham, MA, USA 2014.

[50]. Grimsmo EL, Aalberg A, Langseth M, Clausen AH. Failure modes of bolt and nut assemblies under tensile loading. Journal of Constructional Steel Research 2016;126:15-25.

[51]. Li D, Uy B, Wang J, Song Y. Behaviour and design of high-strength Grade 12.9 bolts under combined tension and shear. Journal of Constructional Steel Research 2020;174:106305.

[52]. BS EN ISO 898-1:2013 Mechanical Properties of Fasteners Made of Carbon Steel and Alloy Steel-Part 1: Bolts, Screws and Studs with Specified Property Classes–Coarse Thread and Fine Pitch Thread. British Standard Institution 2019.

[53]. Lee J, Fenves GL. Plastic-damage model for cyclic loading of concrete structures. Journal of engineering mechanics 1998;124:892-900.

[54]. Lubliner J, Oliver J, Oller S, Onate E. A plastic-damage model for concrete. International Journal of solids structures 1989;25:299-326.

[55]. CEB-FIP 2010. Fib Model Code for Concrete Structures 2010. Ernst & Sohn, Wiley 2013.

[56]. CEB-FIP 1990. Model Code for Concrete Structures 1990. Ernst & Sohn, Wiley 1993.

[57]. Birtel V, Mark P. Parameterised finite element modelling of RC beam shear failure. ABAQUS users' conference 2006.

[58]. Song Z, LI R, Qian m, Shi W, Qian K, Ma H, Chen Q, Zhang G. Optimizing Prestress of Fatigue Property-dominated 8.8-grade Bolts. Chinese Journal of Material Research 2019;33:629-634.

[59]. Li D, Uy B, Wang J, Song Y. Behaviour and design of Grade 10.9 high-strength bolts under combined actions. Steel Composite Structures 2020;35:327-341.

[60]. Yang F, Liu Y, Xin H, Veljkovic M. Fracture simulation of a demountable steel-concrete bolted connector in push-out tests. Engineering Structures 2021;239:112305.

[61]. Finney EA. Structural design considerations for pavement joints. Journal of the American Concrete Institute 1956;28:1-28.